CHARACTERIZING COASTAL SETTINGS USING TEMPORAL & SPATIAL VARIATIONS IN ELECTROMAGNETIC INDUCTION SIGNALS

A Thesis

by

KYLE JORDAN CUNNINGHAM

Submitted to the Office of Graduate and Professional Studies of
Texas A&M University
In partial fulfillment of the requirements for the degree of

MASTER OF SCIENCE

Chair of Committee,	Mark Everett
Committee Members,	Peter Knappett
	Gretchen Miller
Head of Department,	Michael Pope

May 2018

Major Subject: Geology

ABSTRACT

Electromagnetic induction (EMI) methods have long been used to explore and analyze near-surface geological and hydrological components of coastal systems. However, there have been few studies that use EMI to analyze the spatiotemporal hydrodynamics of coastal systems and its relationship to the underlying framework geology. Here the objectives are to investigate the tidal influence on hydrodynamics of coastal systems, compare results with those found in previous studies, and serve as a guide to the methodology and analysis techniques that can be utilized in similar studies and how to interpret the geophysical data. Analyzing the spatiotemporal hydrodynamics, through EMI signal variations, of two coastal settings, Sargent, TX and Matagorda, TX, gives useful information on how groundwater flow is influenced by tidal fluctuations. It has been observed in previous studies that while the tidal signature displays a sinusoidal pattern, the EMI data should follow and step-like function.

Time series and spatial profile data were collected using a portable multi-frequency profiler, at two sites within the Sargent site, the beach and a saltmarsh located on the other side of the Gulf Intercoastal Waterway, and at Matagorda beach. By collecting apparent conductivity measurements at a fixed location, time series data were obtained and then were compared to the appropriate tidal chart, giving information on how groundwater flows in relation to tidal variation. Spatial profiles were conducted in the Sargent saltmarsh and Matagorda beach locations to observe how apparent conductivity varies across the areas. Measurements for spatial profiles were collected twice along each transect.

Data was analyzed through several techniques. Plotting the apparent conductivity measurements from time series and spatial profile data, allows comparison to the tidal charts for

EMI-tide correlations. Fourier and fractal analysis was conducted on spatial profiles only, in order to determine if the original signal can be classified as fractal-like and gain information about the heterogeneity of the subsurface. Lastly, wavelet analysis was applied as a pictorial way of analyzing how the wavenumber content of a signal varies along a profile.

After comparison with results from previous studies, it was found the results here are inclusive in observing a step-like function from the EMI signal data. This was caused from data sets being lost from instrument malfunction, and data being collected over a brief window of the tidal cycle. However, the data collection methods, analysis techniques, and interpretations of data utilized here, serve as an informative guide for future research in similar areas.

ACKOWLEDGEMENTS

I would like to thank my committee chair Dr. Mark Everett, and my committee members, Dr. Peter Knappett, and Dr. Gretchen Miller for their support and guidance. Dr. Everett has provided an immense amount of encouragement, insight, and assistance in data collection for this project.

I would also like to thank my family, Chris, Lisa, Carley, and Christopher Cunningham, along with friends for their encouragement, love and support.

CONTRIBUTORS AND FUNDING SOURCES

This work was supervised by a thesis committee consisting of Dr. Mark Everett (advisor) and Dr. Peter Knappett of the Department of Geology and Geophysics and Dr. Gretchen Miller of the Department of Civil Engineering.

All work for the thesis was completed by the student, under the advisement of Dr. Mark Everett of the Department of Geology and Geophysics.

There are no outside funding contributions to acknowledge related to the research and compilation of this document.

TABLE OF CONTENTS

Page

LIST OF TABLES

TABLE Page

LIST OF FIGURES

1. INTRODUCTION

Coastal systems have been studied in numerous geological and geophysical contexts including hydrological, environmental, and engineering site evaluations. Geophysical methods and instruments allow the opportunity to explore coastal systems in a unique way by non-invasively investigating the subsurface component. One geophysical method, electromagnetic induction (EMI), is being increasingly utilized due, in part, to the recent growth in popularity of portable multi-frequency EMI profilers for near-surface applications. In an EMI survey, the most relevant physical property is the electrical conductivity, sensed by the reception of a time-varying magnetic and/or electric field. EMI measurements respond mainly to the bulk subsurface electrical conductivity (West and Macnae, 1991; Everett, 2013). The electrical conductivity structure of the subsurface, as determined from EMI measurements, can be interpreted in terms of a wide variety of potential targets and application areas, see Table 1.1 (Everett, 2013).

Resistive Targets	Intermediate Targets	Conductive Targets
Permafrost zones	Faults, fracture zones	Seawater intrusion
Aggregate deposits	Archaeological structures	Saline and inorganic plumes
Crystalline rock	Precision agriculture	Clay lenses, claypan soils
Caves, karst	Freshwater aquifers	Pipelines, steel drums, UXO

Table 1.1. *Application areas and targets of EMI geophysics (reprinted from Everett, 2013).*

Sensitivity of the measurements to pore fluid type, in particular conductive seawater intrusion, are a couple of the leading reasons why the EMI method is a useful tool for investigating coastal systems.

1.1 Coastal Systems Background

Exhibiting attributes of both terrestrial and marine environments, coastal systems are spatially complex and temporally dynamic across many scales. Coastal environments may contain many different components including beach and nearshore systems, barrier systems, and saltmarshes, along with coastal sand dunes, coral reefs, and atolls, to name a few, although the latter-mentioned systems are outside the scope of this thesis. Coastal environments are highly susceptible to changes from a myriad of factors. Everything from waves, tides, winds, and storms to geological and ecological factors to human interaction, can all have an affect on coastal systems. Due to the wide range of factors influencing the coast, different classification schemes have been developed, depending on the scale of the region being investigated. For example, on a local scale (about 10-100m) coasts are generally classified by single parameters such as wave or tidal environment, while on broader scales (>100m), classifications using geology or tectonic settings are preferred. Although various classification schemes have been proposed, a standard subdivision of the coastal zone exists (Fig 1.1).

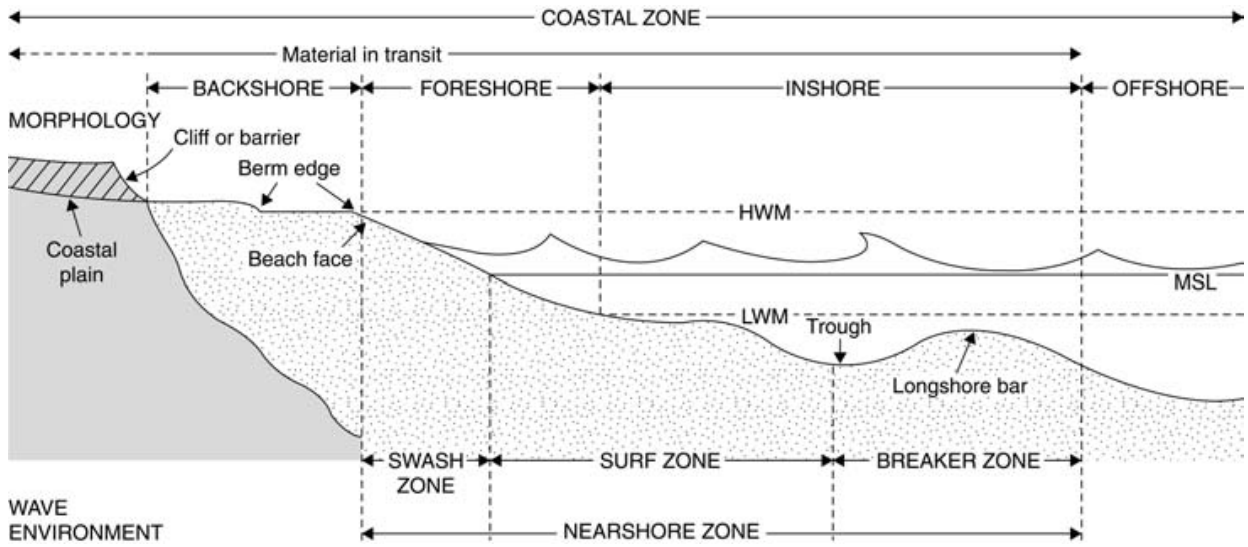

***Figure 1.1**: Subdivision of the coastal zone using both morphological and wave process terminology (reprinted from Haslett, 2009).*

Two sets of terms are shown in Fig. 1, one subdivides the coastal zone based on morphological boundaries (backshore, foreshore, inshore, and offshore), while the other is based on the types of wave processes that operate (swash zone, surf zone, and breaker zone, which together compose the nearshore zone) (Haslett, 2009).

Barrier systems comprise some of the most dynamic coastal landforms, being strongly influenced by storms and changes in depositional supply of sediment. Coastal barriers are linear depositional landforms separated from the mainland by a bay, lagoon or marsh (Davidson-Amott, 2010). These landforms act as a barrier, protecting the mainland from potentially destructive processes operating on the open ocean, by reducing wave and storm impact. In the shore-perpendicular direction, the barrier system consists of inner-shelf, nearshore, beach, barrier and lagoon backbarrier sub-environments; while the sub-environments in the alongshore direction include the barrier system, tidal inlets, and subtidal deltas (Weymer et al., 2015). Barrier systems are commonly thought of as barrier islands, completely separated from the mainland, but not all barrier systems follow this pattern. There are three primary classifications of barrier systems depending on their geometry: (1) no free ends, which include tombolos and other barriers built across a bay and estuary from one shore to another; (2) one free end, that includes a range of spit forms and cuspate forelands forming where there is a convergence of littoral drift, resembling a peninsula; and (3) two free ends, which is a barrier island that is not connected to the mainland shore on either end, see Fig 1.2 (Davidson-Amott, 2010).

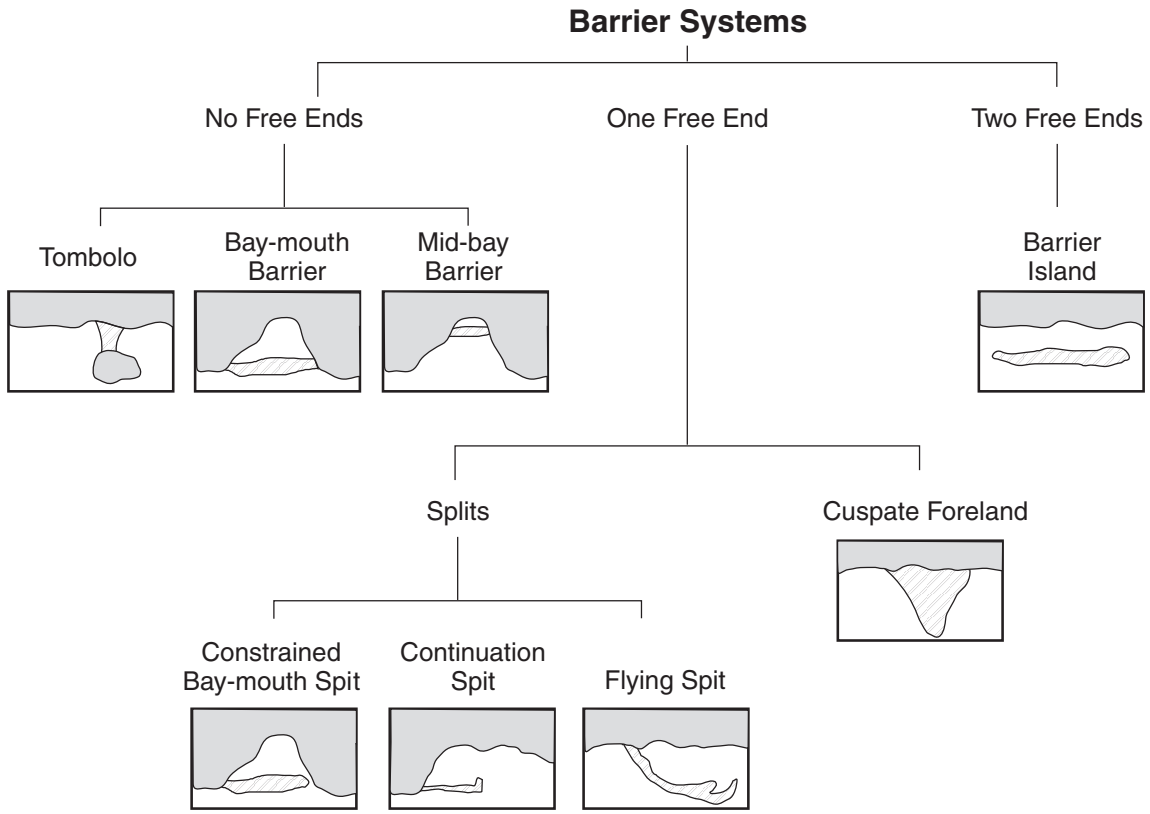

***Figure 1.2**: Classification of barrier systems based on morphology and geometry (reprinted from Davidson-Amott, 2010).*

Although generally investigated for ecological purposes, from a physical standpoint salt marshes are highly dynamic systems within the coastal environment. Forming in the intertidal zone of sheltered coasts, saltmarshes enable the growth of vegetative habitats due to the reduced wave energy. Despite experiencing reduced wave energy due to the shelter from the open ocean, saltmarshes are always influenced by tidal currents (Callaghan et al., 2010). Morphologically, saltmarshes consist of a gently sloping vegetated platform, dissected by a network of tidal creeks (Davidson-Amott, 2010). As high tide begins to rise, so does the water level in the tidal creeks and as the tidal creeks fill, the water eventually flows onto and inundates the marsh. As the tidal cycle continues, the water in the creeks will drain as low tide pulls the water back out toward the sea. Depending on the tidal range and location of the saltmarsh, the intensity or the amplitude of

the hydrodynamic tidal cycle will vary. Saltmarshes in areas that experience high tidal ranges will be subject to more intense hydrodynamic processes than those with low tidal ranges.

Coasts, like other natural environments, can be viewed as geological systems characterized by inputs and outputs of energy, such as wave or tidal energy, and a material balance, such as sediment deposition or erosion (Haslett, 2009). Increases or decreases in energy or changes in the material balance cause a morphological response, as the coast attempts to return to its natural state of equilibrium. Understanding the effects that increases or decreases in energy have on the system morphology is vital to understanding the system as a whole. An important process is saltwater intrusion into fresh groundwater (which defines the freshwater-saline water interface), while an important cause-and-effect relationship is that between tidal fluctuations and groundwater level.

Over 100 years ago it was discovered that, like freshwater, salt water not only exists at Earth's surface, but also beneath it. The underground salt water resides at a depth below sea level of about 40 times the height of the freshwater table above sea level (Todd and Mays, 2005). This distribution of fluids marks the fresh-saline interface which is described by the Ghyben-Herzberg principle,

$$z = \frac{\rho_f}{\rho_s - \rho_f} h_f$$

where ρ_f is the density of fresh water, ρ_s is the density of saline water, h_f is the elevation of the water table above sea level, and z is the depth of the fresh-saline interface. This relation can be seen in Fig 1.3 as an idealized sketch of an unconfined coastal aquifer.

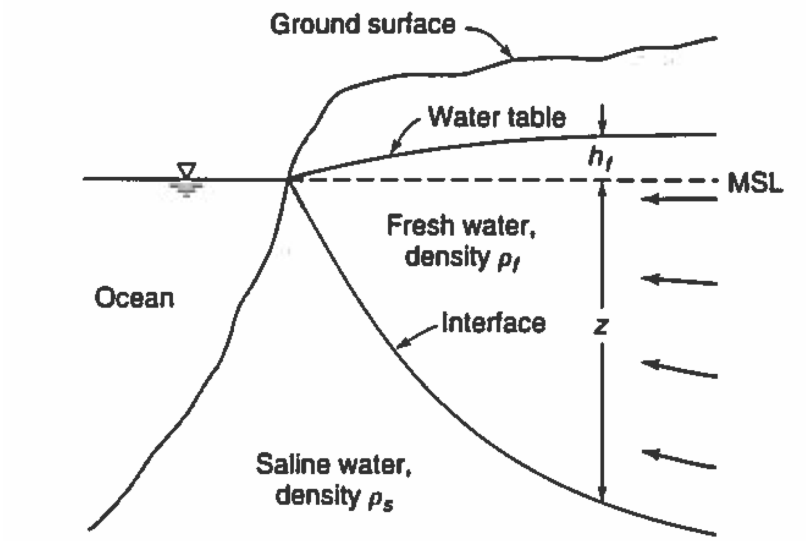

***Figure 1.3**: Idealized sketch of occurrence of fresh and saline ground-water in an unconfined aquifer (reprinted from Todd and Mays, 2005).*

One can see that the fresh-saline interface is at the surface where the ocean meets the land, but becomes progressively deeper with distance inland. However, such a sharp interface is idealized and does not naturally occur. Instead, a brackish transition zone separates the two fluids, see Fig. 1.4 (Todd and Mays, 2005).

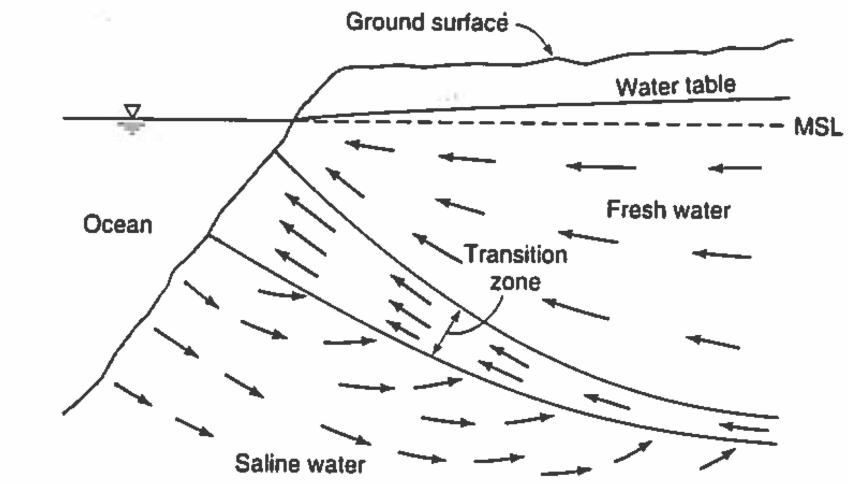

***Figure 1.4**: Vertical cross section showing flow patterns of fresh and saline water in an unconfined coastal aquifer (reprinted from Todd and Mays, 2005).*

In the subsurface the fresh water flows seaward, while the saltwater flows landward, this causing mixing within the transition zone. However, this is an idealized scenario, whereas actual groundwater flow properties are related to and influenced by tidal dynamics among other factors.

The relationship between tidal fluctuations and coastal groundwater dynamics is spatially and temporally complex. It has been shown in previous studies that the fluctuation and position of the water table beneath sandy beaches is heavily influenced by tidal cycles (e.g., Lanyon et al., 1982; Nielsen, 1990; Ataie-Ashtiani et al., 2001). Nielsen (1990) first observed that the minimum water table level is substantially higher than the low tide level and the mean water water table level is higher than the mean sea level. Based on field measurements made of water table heights inside a beach which had no significant wave activity or outflow of rainwater and thus exhibited tidal effects in pure form, Nielson noted that this superelevation is due to three mechanisms: formation of a beachfront seepage face around low tide, asymmetry of the boundary condition at the sloping beach face, and finally the nonlinearity of the governing equations (Darcy's law, continuity equation, and Boussinesq's equation). A further observation from Nielsen (1990) was, even though the tidal cycle fluctuates in time in a roughly sinusoidal manner, the temporal variation in the water table is far from sinusoidal; the rise is much steeper than the decline and the lag of low water table behind low tide in the ocean is longer than the lag of high water table behind high tide. This phenomenon arises because the beach slope acts as a filter such that infiltration at high tide is more efficient at groundwater transport than drainage at low tide. In other words, although the surface tidal signal exhibits a periodic trend, the groundwater flow and water table follow a more step-like pattern. The step-like behavior has been inferred from EMI geophysical time-series data by Weymer et al. (2016).

1.2 EMI Applications in Coastal Settings

Geophysical methods have long been used to explore and better understand the unseen subsurface component of coastal systems (Nielsen 1990 and 1999; Cartwright and Nielsen 2001; Horn 2002 and 2006). Common geophysical methods applied to coastal studies include electrical resistivity tomography (ERT), seismic reflection and refraction, ground-penetrating radar (GPR), and electromagnetic induction (EMI). In the past several years there has been rapid growth in the use of EMI geophysics and the literature on such studies is extensive (e.g. Everett and Farquharson, 2012). EMI studies have covered everything from modeling and inversion (e.g. McNeill, 1980; Santos et al. 2010) to identifying unexploded ordnances (UXO) (Everett, 2013) to archaeological site investigations (Pincus et al., 2013) and coastal systems analysis (Sejimonsbergen et al., 2004; Vrbancich, 2009; Christensen and Halkjaer, 2010; Nenna et al., 2013; Delefortrie et al., 2014; Weymer et al., 2016). EMI geophysical studies may be carried out in different configurations depending on the target of the investigation. For example, EMI studies can employ multiple sensors either equally spaced or spaced at varying distances, airborne platforms (e.g. Vrbancich, 2009), or terrain conductivity profilers. While operating in the frequency- domain is more popular, certain complications and difficulties using this procedure, such as separating the EM field into primary and secondary parts, have led to the use of time- domain electromagnetic techniques, which are used primarily to delineate layered structures in applications such as oil and groundwater exploration (Nabighian and Macnae, 1991).

EMI geophysical methods have been used to support a number of applications in coastal settings, including groundwater resource management (Nenna et al., 2013), classification of coastal wetlands (Paine et al., 2004), and the relationship between subsurface conductivity and

the underlying geologic framework (Seijmonsbergen et al., 2004). However, there have been very few studies, other than Weymer et al. (2016), that use EMI to analyze the spatiotemporal hydrodynamics of coastal systems and its relationship to the underlying framework geology.

1.3 Objectives

The primary objective of this study is to investigate the tidal influence on hydrodynamics of coastal systems, using temporal and spatial variations in EMI signals at two locations, Sargent, TX and Matagorda, TX. Results found at these sites will be compared to those found in a similar, previous study at Padre Island National Seashore, TX by Weymer et al. (2016). The methodology is to obtain time-series and spatial profiles (longitudinal transects) of varying EMI signals from the two study areas, and then to determine if it is possible to detect tidally fluctuating water tables using EMI in the coastal environments. Once the data is obtained, wavelet, Fourier, and Fractal analysis will be conducted in order to interpret the data. If successful, in regards to coastal management, ecological, and recreational purposes, there will be a better understanding of the implications of the groundwater dynamics and tidal quiet response time (daily variation) of the coast in absence of storms.

2. GEOLOGICAL SETTING

The geological setting for this project consists of two study areas along the Texas coastline, which is referred to as "Sargent" and "Matagorda Peninsula". The Sargent area comprises two locations, the beach and a salt marsh just landward from the intercoastal waterway, while the Matagorda Peninsula area was studied along the beach only. While both study areas can be classified as barrier systems, they differ in composition as well as having minor differences in geologic history, which could influence the hydrodynamics of the system such as amplitude and frequency of tidal fluctuations. The following sections describe the two study areas as well as their geological history.

2.1 Sargent, Texas

Sargent is located southwest of Galveston Island in the central portion of the Texas Gulf coast, on the western flanks of the Brazos River paleodelta (Stauble et al., 1994). Positioned in-between San Bernard River and Caney Creek (Fig. 2.1), two sites of interest have been identified within the Sargent area, one is the beach itself and the other is a salt marsh located on the northern side of the intercoastal waterway ~0.4km landward from the beach (Fig. 2.2).

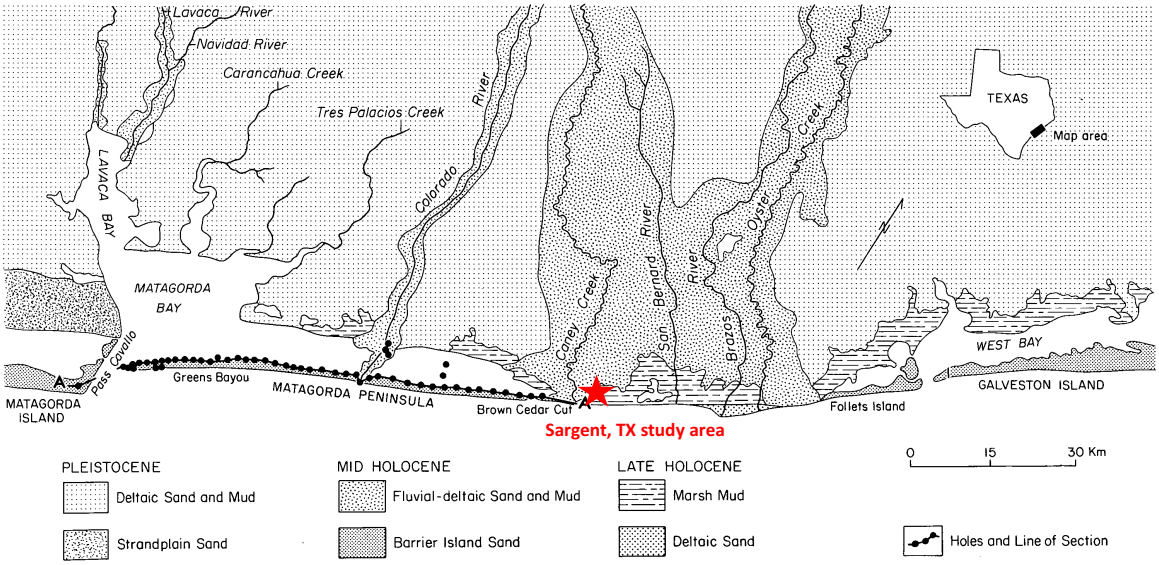

***Figure 2.1**: Map location of Sargent, TX, represented by the star (adapted from Wilkinson and Basse, 1978).*

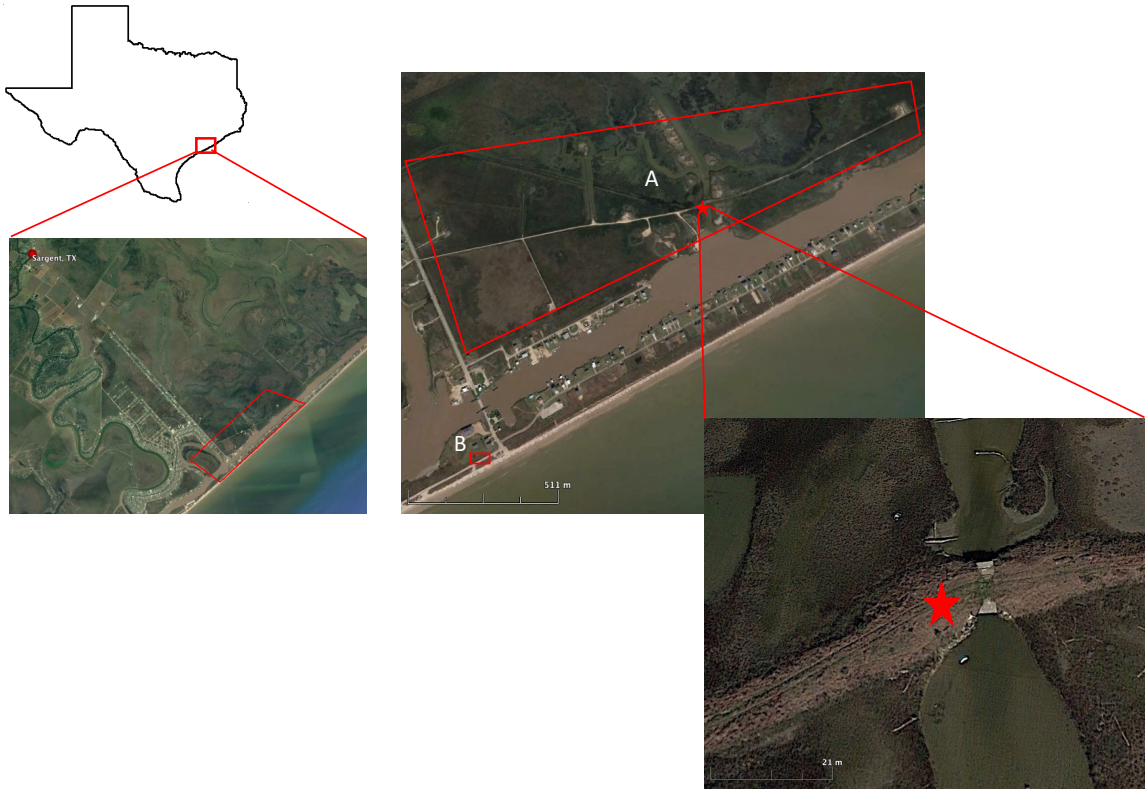

***Figure 2.2**: Site map of Sargent, TX area. (A) Saltmarsh location; the star marks the the levee for the time-series data collection. (B) Beach location (Google Earth).*

Here, the beach is comprised of a thin, sandy top layer ~5-10 cm depth extent, underlain by a thick, reddish-brown deltaic mud substrate that can be seen outcropping in certain portions of the beach. The Colorado-Brazos River fluvial-delta complex, which includes the Brazos River, Oyster and Caney Creek, and the San Bernard River, is the primary sediment source for this beach system (Weiss and Wilkinson, 1988). Sargent beach is a narrow beach compared to others in Texas, spanning only ~10-15 m from the shoreline to the first zones of vegetation and, like most other Texas beaches, experiences daily micro-tidal fluctuations, with the tidal range not exceeding 2 m. The specific location along Sargent beach that was investigated is located just

southwest of the Intercoastal Water Swing Bridge, ~20 m off highway FM 457 on the seaward side. Present Sargent beach is an island, functioning as a barrier to the open ocean, and was created in 1949 when the dredging of the intercoastal waterway was complete, through the deltaic headland (Stauble et al., 1994).

The second location in the Sargent study area is a salt marsh, located north-northwest of the intercoastal, east of highway FM 457. The salt marsh site is primarily composed of the same reddish-brown deltaic mud, but with a thin layer of top soil vegetated by cordgrass (*Spartina spartinae*). Cross-cutting engineered levees offer accessibility to easily navigate this site for data collection along the canals traversing throughout the salt marsh. Due to the close proximity to the beach, this site also experiences daily micro-tidal fluctuations, as do most Texas beaches.

The near-surface geology of the Sargent area originates from a series of complex glacial and interglacial climate and sea-level changes and can be divided into three parts, the Pleistocene, Holocene, and modern. Beginning about 50,000 – 60,000 years B.P. (before present), sea level began dropping in response to final episodes of Wisconsin glaciation (McGowen et al., 1976). As sea level dropped, rivers and streams began eroding the underlying Pleistocene fluvial and deltaic bedrock. Deep valleys were cut and new deltas began to form from rivers such as the ancestral Brazos and Colorado at about 30,000 B.P. when sea level reached its minimum value, 135 m below present level (McGowen et al., 1976). These prograding deltas deposited river, delta, and reworked marine facies out on the continental shelf, marking the end of the Pleistocene.

The beginning of the Holocene saw sea level begin to rise to its present-day level. Sea level rose until present mean sea level (MSL) was reached from about 18,000 – 2,800 years B.P., as valleys carved by the ancestral Brazos and Colorado Rivers became filled by fluvial, deltaic,

estuarine, and marine deposits (McGowen et al., 1976). At the same time the valleys were being filled and sea level was rising, the Brazos – Colorado estuary was forming, until present MSL was reached. This prompted a prograding delta from the Brazos and Colorado Rivers, filling the estuary water body over an area of approximately 57 km^2 to the present shoreline ending the Holocene (McGowen et al., 1976).

As the estuary filled, the Brazos and Colorado Rivers, along with smaller meandering stream systems, discharged sediment out to the Gulf of Mexico. The modern and historical processes of erosion, deposition, compaction, and subsidence have shaped the Sargent area to its present state and are still at work today.

In summation, according to McGowen et al. (1976), five principal natural changes began along the coast when sea level approached its present level: (1) the Brazos and Colorado bayhead deltas rapidly filled their estuaries; (2) walls of smaller bays were eroded and their bay margins expanded; (3) headward erosion by short streams continued within Pleistocene interdistributary areas; (4) Matagorda Peninsula, and small valleys to the west were flooded, forming bays; and (5) marshes developed on the distal part of the Holocene-Modern Brazos-Colorado delta plain, on former mudflats, and within drowned drainage systems.

In recent history, there has been a major increase in anthropogenic disturbance of the natural system at Sargent such as dredging the intercoastal waterway, hydrologic engineering and oilfield operations. The main disturbance of this area was the dredging of the intercoastal waterway. As the intercoastal water continued to be dredged, moving south along the Texas coast, it went through Sargent. Following the path from the San Bernard River delta, the intercoastal created an island between Sargent's coast and the Gulf of Mexico. This island is now Sargent beach and acts as a barrier system protecting the coast line from storms and wave

processes (Fig. 2.2). Being a barrier system and separated from the mainland, the beach will have different hydrodynamic processes than the saltmarsh. Sargent beach experiences more drastic wave action and blocks the saltmarsh from these waves. The dredging of the intercoastal changed the natural system in way where it was once a connected shoreline, but now is a saltmarsh protected by the beach barrier system and separated by the canal. The saltmarsh still experiences tidal fluctuations since the intercoastal waterway connects to the gulf, although it is a more delayed response than seen at the beach face.

While the beach was more directly affected by the dredging of the intercoastal, the natural system of the saltmarsh has been disturbed in other ways such as engineering and oilfield operations. A series of cross-cutting levees was engineered throughout the saltmarsh to provide easy accessibility in the area. As a result of constructing the levees, a system of canals formed. The need for these levees resulted from the desire to extract resources in the saltmarsh, mainly oil and natural gas. Once the levees were constructed, field operations were put in place to extract these minerals, and pipelines were put in place for transportation. These pipelines were both buried beneath and laid along the surface of these levees. The construction of levees and oilfield operations, further disrupted the natural system of the saltmarsh. The saltmarsh now has levees, which alter the natural tidal flow through the system of canals that formed.

2.2 Matagorda Peninsula

The Matagorda Peninsula is a narrow, shell-rich barrier separating the Gulf of Mexico from Matagorda Bay (Wilkinson and Basse, 1978), ~38km southwest of Sargent in the Colorado River delta. The Matagorda study area is located in the central portion of the Matagorda Peninsula, ~2km northeast of FM 2031, on the beach face (Fig. 2.3).

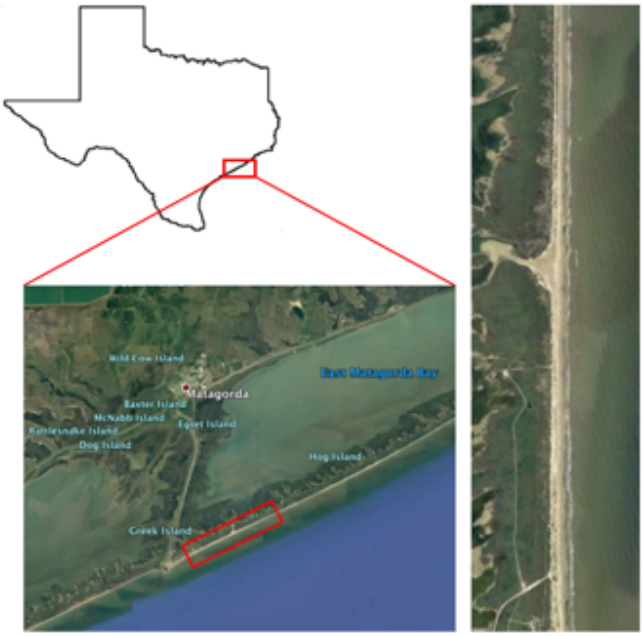

***Figure 2.3**: Site map of Matagorda Peninsula area (Google Earth).*

The beach face is composed of shell-rich sand down to a depth of ~6m, which is underlain by estuarine mud, and experiences daily micro-tidal fluctuations. Matagorda Peninsula's primary source of sediment deposition and rock fragments was Pleistocene fluvial-deltaic deposits discharged by the Brazos – Colorado River systems.

Although formed after Sargent, Matagorda Peninsula has a nearly identical geologic history in that it recorded a series of complex transgressions and regressions throughout the Pleistocene and Holocene. During the Pleistocene, sea level began to drop, which gave rise to erosion and deep valleys cut through the underlying fluvial and deltaic bedrock by rivers, such as the Brazos and Colorado, and other smaller streams. This regression also allowed the Brazos and Colorado Rivers to create new deltas while filling in these valleys with river and deltaic sediments. During the Holocene, as the valleys continued to fill, sea level began to rise creating

the Brazos-Colorado estuary. The Brazos and Colorado Rivers, then prograded a delta across this estuary, filling it with deltaic sediments.

Following the filling of the estuary, meanderbelt systems transported sediment to small deltas, forming shoals in the open Gulf of Mexico (McGowen et al., 1976). Discharge from the Brazos and Colorado Rivers also provided sediment, which became the primary source for longshore drift. At this time, a spit attached to the Brazos – Colorado deltaic headland began to accrete to the southwest and ultimately coalesced with shoals to form the Matagorda Peninsula (McGowen et al., 1976). The continuation of longshore drift deposition, erosion, and compaction have influenced the current state of the Matagorda Peninsula and will continue to do so. Due to the higher sand content found at Matagorda, it will experience a higher rate of these processes, than would be expected at the mud-dominated Sargent site.The formation of the Matagorda Peninsula caused a back bay, East Matagorda Bay to form behind it. The Matagorda Peninsula is now separated from the mainland saltmarsh by East Matagorda Bay.

While the intercoastal waterway passes through Matagorda, it is not as significant a perturbation compared to Sargent. This is because the intercoastal is much further inland, on the landward side of East Matagorda Bay. Since, the Matagorda Peninsula beach is on the gulf side and separated from the intercoastal by East Matagorda Bay, the disturbance caused by the dredging of the intercoastal is not a significant factor for this study.

3. METHODS

The versatility of geophysical instruments (such as EMI profilers), offers many possibilities to investigate the hydrodynamics of a coastal area and its relation to the tidal influence on groundwater flow. Here, a portable mutli-frequency EMI profiler was used to collect data in order to examine the spatially-variable tidal influence on the groundwater hydrodynamics of Texas Gulf coastal systems. Temporal and spatial variations in EMI signals were gathered and analyzed at two locations, Sargent and Matagorda.

3.1 Portable Multi-frequency EMI Systems

Recently, portable multi-frequency electromagnetic induction (EMI) profilers have become a popular tool for near-surface geophysical studies. The profilers are non-invasive, cover large areas within a short time, and are relatively inexpensive compared to other geophysical instruments (Weymer et al., 2016). These portable devices provide users with great flexibility in selecting operating frequencies, sensor height, and coil configuration to optimize the measurement parameters for specific targets and mapping applications (Huang et al., 2008). A typical EMI system contains a transmitter loop coil (TX) and a receiver loop coil (RX), which can either be located at a fixed offset on a rigid connector, of have variable separation distance, in which case TX and RX are connected by cables. The TX carries an alternating current in the loop, which generates a dipolar primary magnetic field. A secondary magnetic field generated by electrical currents induced in the conductive Earth by the time variations of the primary field is sensed by the RX coil (McNeill, 1980).

For the purposes of this thesis, “portable” means a light weight sensor that is operated by one person in a continuous acquisition mode while walking (Weymer et al., 2016). Unlike traditional EMI sensors, portable EMI profilers have a short, fixed distance between the TX and RX coils. The specific multi-frequency EMI profiler used for this study is the GSSI Profiler EMP-400^{TM}, with a TX – RX coil separation distance of 1.2m (Fig. 3.1).

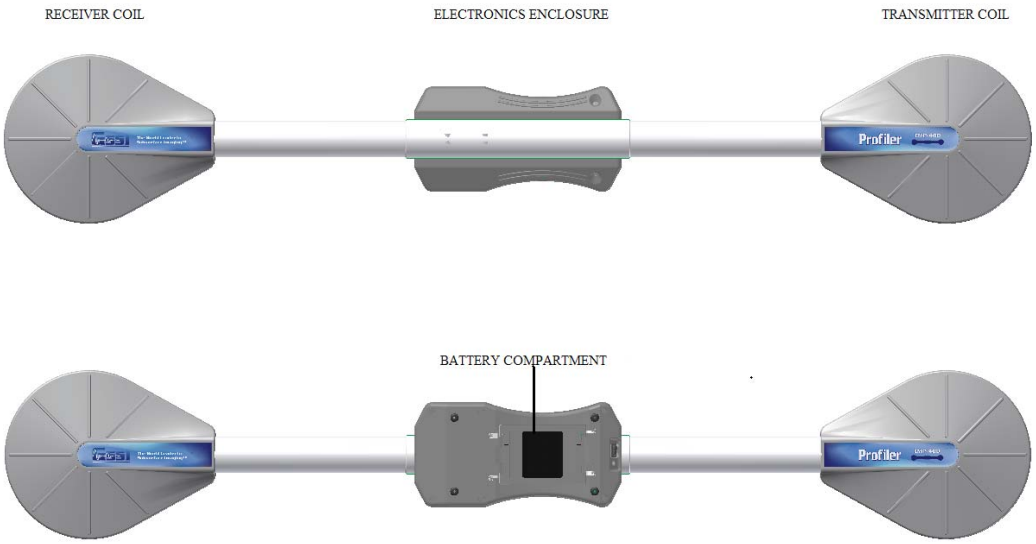

Figure 3.1*: GSSI Profiler EMP-400^{TM} top and bottom view (reprinted from GSSI, 2007).*

The TX has the ability to emit a continuous sinusoidal waveform with frequency ranging from 1 – 16 kHz, selectable by the operator at 1 kHz increments (GSSI, 2007). The RX measures a number of EMI-related quantities, most importantly the In-phase (I) and Quadrature (Q) responses (Won et al., 1996) This system, then measures apparent conductivity (σ_a) in mS/m by transformation of the raw quadrature response according to the formula

$$\sigma_a = \frac{4}{\omega \mu_0 s^2} \left(\frac{H_s}{H_p}\right)$$

where $\omega = 2\pi f$, f is frequency, μ_0 is the permeability of free space, s is the intercoil spacing, H_s is the secondary magnetic field at the RX., and H_p is the primary magnetic field at the RX (McNeill, 1980). The Tripod Data Systems (TDS) Recon-400 PDA controls the electronics of the the GSSI Profiler EMP-400™. In addition, the PDA also collects and stores the measurements received by the RX coil and provides GPS coordinates for each measurement, accurate to ~1 m (GSSI, 2007).

With EMI sensors, the separation distance between the TX and RX is important for determining the maximum depth that can be reached, or depth of investigation (DOI), with the greater the separation the greater the DOI. However, since the newer portable EMI profilers have a short, fixed separation distance, but commonly operate on multi-frequency domains, the DOI can be controlled by changing the frequencies. The DOI for a given frequency is determined by many factors, such as sensor sensitivity, precision, ambient noise levels (Huang, 2005), and the physical properties of the subsurface, mainly the electrical conductivity (Everett, 2013). As frequency increases, the depth of signal penetration decreases. Thus, the GSSI Profiler EMP-400™ operating its minimum frequency of 1 kHz will provide the deepest depth of penetration while operating at its maximum frequency of 16 kHz provides the shallowest depth of penetration. The DOI is always of the same order as the TX-RX intercoil separation, with lower frequencies penetrating just fractionally deeper than the higher frequencies; in other words, the different frequencies probe only to marginally different depths. The attenuation of a penetrating electromagnetic signal in a conductive medium is known as the skin effect (Huang, 2005). The skin depth δ is the depth at which a plane wave is attenuated by of $1/e$ of its amplitude at the surface, and follows the equation (Huang, 2005; Everett, 2013):

$$\delta = \sqrt{\frac{2}{\sigma\mu\omega}}$$

The data for this thesis were acquired using of the portable multi-frequency EMI profiler, the GSSI Profiler EMP-400^{TM}, at two study areas. Not only does this profiler have the capability to record simultaneous measurements at 3 different frequencies. For the current study, 3 kHz, 10 kHz, and 15 kHz were used. This allowed EMI responses to be collected at low, medium, and high frequencies in order to probe the depth dependence of the geoelectrical structure beneath the study sites. Operating at the three frequencies: 3, 10, and 15 kHz, the DOI can be expected to be in the range of ~6.4-2.1 m, keeping in mind the sensor height since the DOI is under the sensor.

3.2 Data Collection

Time series and spatial profiles of EMI apparent conductivity were collected at the two study areas, Sargent and Matagorda, using different methodologies. The data were then compared to tidal charts obtained from NOAA. In other words, the temporal and spatial changes in apparent conductivity from the EMI measurements were compared to the changes in tide levels reported NOAA. The EMI measurements are expected to respond to variations in the depth of the subsurface water table beneath the beach whereas the tidal charts show the changing location of the surface water level on the shoreline, assuming a quiet sea state.

3.2.1 Time Series

Temporal EMI signal measurements were recorded at both of the Sargent sites, the beach and the saltmarsh, and then at the Matagorda location. These measurements were made to check for possible EMI – tide correlations. The process to collect the time-series data is similar at all locations; the Sargent beach site was the first to be investigated. In order to obtain these data

once on the Sargent beach, the profiler was turned on and the PDA was set to automatically record apparent conductivity at 5 s intervals, simultaneously at each of the three TX operating frequencies: 3 kHz, 10 kHz, and 15 kHz. Once the profiler was on and set to record at the desired parameters, a standard calibration test was performed. This test, as per the GSSI operating manual, is done to calibrate the device to properly record the apparent conductivity at the appropriate sensor height, which in this case was at a height of 0.0 m since the profiler was placed directly on the ground. The profiler and PDA were placed on the foreshore of the beach ~5 m back from the waterline (Fig. 2.2 B) and left to collect data for half a tidal cycle or ~6 hours.

After the Sargent beach time-series were acquired, measurements were made at the Sargent saltmarsh. The data here, was collected by placing the profiler and PDA directly on one of the levees cross-cutting the marsh. A levee was chosen as the measurement site due to its accessibility, and the fact the profiler is not waterproof and so cannot be placed directly in the water. After reconnoitering the marsh area with the profiler turned on and observing spatial variations in apparent conductivity, the location to conduct the time-series, atop a hill on a levee near a bridge abutment (Fig. 2.2 A), was chosen based on its higher resistivity, which should increase the likelihood to see a dynamic EMI response to a tidal cycle. This is because freshwater has a higher resistivity than saltwater, making it easier to observe the changes in the tidal cycle wherein the level of conductive saltwater rises and falls relative to the ground surface. The same procedure, as per the first Sargent site, was followed to set up the profiler and PDA to automatically record apparent conductivity for the same three frequencies at 5 second intervals. The profiler and PDA were left atop the levee to record data for half a tidal cycle or ~6 hours.

The beach and saltmarsh locations were conducted on consecutive days with the beach data gathered on Dec. 14, 2016 and the salt marsh data gathered on Dec. 15, 2016.

The time-series data for the Matagorda site were collected on Dec. 16, 2016. The data collection was conducted in the same manner as at the Sargent beach site. I set the PDA to automatically record apparent conductivity measurements at 5 second intervals for three frequencies; 3 kHz, 10 kHz, and 15 kHz. The profiler was calibrated in the same manner as at Sargent beach. However, at the Matagorda location, the profiler and PDA were placed a significantly farther back from the waterline, about 35m onto the foreshore, landward of the beach face. The profiler was left to collect data for slightly less than half a tidal cycle or ~2 hours.

3.2.2 Spatial Profile

Spatial variations in EMI apparent conductivity were measured and recorded using the Profiler EMP-400^{TM}. These measurements allow the the comparison of spatial variability in apparent conductivity between two different coastal settings, Sargent and Matagorda, and also a comparison to the earlier results found at Padre Island National Seashore (see Weymer et al., 2016). The spatial profile data was gathered in a different manner than the time-series data, since spatial acquisition requires more intensive, hands-on field work.

After site visits were made at both the beach and saltmarsh sites in Sargent, to determine whether spatial profiles should be conducted, it was determined that a spatial profile was only necessary in the saltmarsh. This selection was made because Sargent beach has thick mud substrate that can be seen outcropping in portions of the beach. The electrically conductive mud

has an attenuating effect on the EMI responses. A single spatial profile was therefore conducted along the cross-cutting levees in the saltmarsh spanning an area just over 0.05 sq. km (Fig. 3.2).

Figure 3.2*: Route traveled for spatial profile in the saltmarsh at Sargent, TX, highlighted in reed in the lower right corner (Google Earth).*

For these measurements, the PDA was set to automatically record apparent conductivity at 2 s intervals to obtain high-resolution data, at the same three frequencies; 3 kHz, 10 kHz, and 15 kHz. After calibrating the profiler while holding it about 0.2m above the ground, the height the profiler was carried for the spatial profile, I walked along the predetermined paths at normal walking pace, ~4.8 km/hr. Data measurements were recorded while walking twice along each path. Such a duplicate recording of the data allowed evaluation of repeatability of the measurements.

At the Matagorda location, the process of obtaining the EMI-apparent conductivity spatial profile was very similar to that of the saltmarsh. However, here, the PDA was set to automatically record apparent conductivity at 1 second intervals using the same three frequencies. Setting the recording interval lower provides a higher-resolution dataset. The profiler was calibrated on the shoreline, directly at the waterline, while held at a height of 0.2 m, so it will be properly calibrated to record the prevailing geologic and hydraulic conditions. While holding the profiler at the height of 0.2m, I walked along the shoreline a distance of 3.6 km (Fig. 3.3).

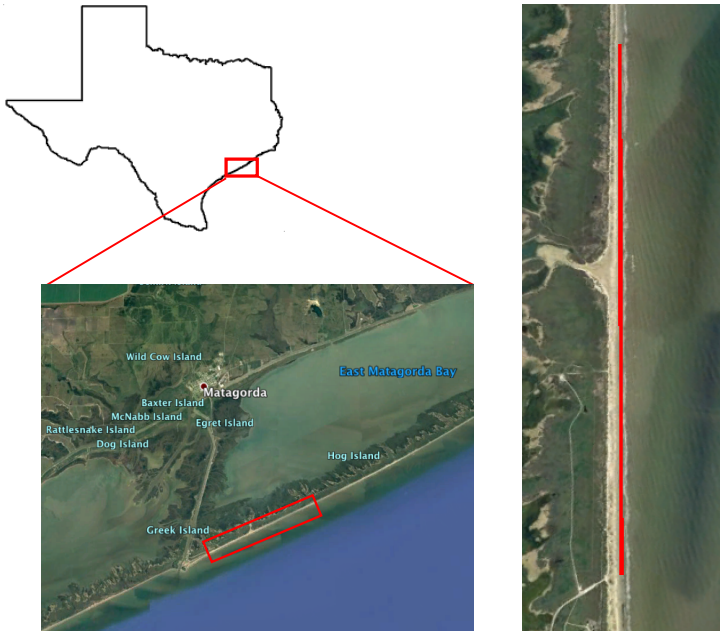

***Figure 3.3**: Path for spatial profile, highlighted in red on the right side, at Matagorda beach, TX. (Google Earth).*

This path length was chosen because it could be walked in a couple of hours, while collecting alongshore data across a substantial yet representative portion of the beach. Measurements were recorded the entire length of the path heading in one direction. After about an hour long break,

measurements were recorded walking back along the same path. As at the Sargent saltmarsh, duplicating these measurements allows to test for repeatability.

4. ANALYSIS & RESULTS

Analyzing data is a critical step in any study, after data collection is finished, in order to explore implications and draw conclusions. In the present study, the data were analyzed using different software tools such as Microsoft Excel and Rstudio, and different techniques such as wavelet, fractal, and Fourier analysis. The procedures detailing how each of these techniques were implemented, the results, and the corresponding interpretations drawn from the analysis are explained in the following sections.

4.1 Implementation of Time Series and Spatial Profile Analysis

The first step in analyzing a data set after it is downloaded from the EMI Profiler PDA to a computer is to save it in a format (.csv) that can be read by Microsoft Excel software. For each study site, I maintained separate file storage locations for the time-series analysis and spatial profiles data sets, in order to keep track of which data set belonged to which location. Once the data sets were converted to Excel files, I plotted the apparent conductivity measurements for all three frequencies against their record number. For the time-series data, this shows how the apparent conductivity changed over time at a fixed location, while for the spatial profiles it shows how the apparent conductivity varies along the walked transects within the study area. A comparison of the variations in these plots to the appropriate tidal chart, obtained from NOAA [www.tidesandcurrents.noaa.gov], gives potentially useful information about how the groundwater flows under the influence of tidal variations relative to the nominal location of the waterline. The tidal chart prescribes the variation in the nominal location of the waterline whereas the apparent conductivity reading presumably tracks the elevation of the saline

groundwater table and/or the saline-fresh groundwater interfaces beneath the EMI instrument. The tidal charts are located in the Appendix.

Next, I used the spatial profile data sets to examine the repeatability of the measurements. Spatial profiles were acquired for the Sargent saltmarsh and Matagorda sites. To test for the repeatability, separate graphs were created for each frequency and for each levee (note that spatial profiles can be segmented into data acquired along individual levees, as the entire profile is a composite of data acquired along several different levees). In other words, for each levee at the saltmarsh site, a separate graph was created for each frequency; thus each levee is characterized by three different repeatability graphs. These graphs were created by taking the apparent conductivity measurements of one frequency, along one particular levee, cutting it in half and then reversing the order of the second half around. This is done because the data were acquired by walking in both directions (i.e. "there and back") along a levee. The two halves of data were then plotted on the same graph to show the correlation of the measurements from the two walking directions. This process was done for each frequency along each levee in the saltmarsh, as well as for the single "there-and-back" profile at the Matagorda location. All time-series, spatial profiles, and repeatability graphs at both sites in the Sargent location and at the Matagorda location can be found in the Appendix.

At the Sargent beach location, the time-series data plots showed very little variability for any of the three frequencies (A-6). The only frequency to show variation of significance is 3 kHz, which recorded an increase in apparent conductivity of ~10 mS/m over the time span of the measurements. This data set file was acquired in the late afternoon approximately 3:30-5:30 p.m. The increase in 3-kHz apparent conductivity correlates to the rising tide evident on the tidal chart, which shows that high tide occurred at approximately 9 p.m. in the evening. The other two

frequencies, 10 kHz and 15 kHz, do not show any significant change in apparent conductivity. This observation can be explained by the fact that signals at higher frequencies penetrate to shallower subsurface depths than do the 3 kHz signals. The beach at Sargent is characterized by a thin surficial layer of sand underlain by mud which outcrops in portions of the beach. Since mud has much lower permeability than sand, it is likely that the mud acted as a barrier to the groundwater, preventing its detection by the profiler. It should also be mentioned that, during the data collection process at Sargent beach, there was an issue changing the batteries of the PDA which resulted in a data set file that was lost and found to be unrecoverable. The PDA suddenly running out of power due to a rapid battery drain is a known issue with the instrument. The lost data set was acquired during the early afternoon, from about 12:30-3:30 p.m., so that I have no information about the temporal variation of apparent conductivity at any frequency during that time interval.

The time series acquired at the Sargent saltmarsh site, showed more variation. Data collection for this site started at low tide in an attempt to capture an increase of apparent conductivity with the rising tide. The first segment of data does not display any significant variation in apparent conductivity, as the measurements on all 3 channels remain relatively constant. However, again at this site a data set file was lost while changing the batteries for the PDA. The lost data set was a key data set that potentially could have shown an increase in apparent conductivity with the rising tide. Weymer et al. (2016) observed a step-like increase in EMI response interpreted as due to a sudden rise in groundwater during a rising tide. If this interpretation holds for the present study area as well, the data which would show this sudden response was missed. The would have been the middle data set that was collected during the early afternoon, but lost.

The second data set that was collected and graphed is marked by the spike on the graph (A-7) and was acquired during the late afternoon (~3:00-5:00 p.m.). The spike in the data is an anomaly that was intentionally caused to test the sensitivity of the profiler to metal objects. As the profiler started collecting data, car keys were placed next to it to observe the change in readings. The spike should not be taken into account for hydrogeophysical interpretation.

The initial apparent conductivity measurements for this data set are ~90 mS/m (3 kHz signal) and ~70 mS/m (10 kHz and 15 kHz signals) higher than the previous recorded data set, which agrees with expectations due to the rising tide. The data here show an interesting trend. The 3 kHz response shows a very slight increase in apparent conductivity (~10 mS/m) through time, whereas the 10 kHz and 15 kHz responses show a gradual decrease in apparent conductivity (~25 mS/m). There are a couple of possible explanations for this.

The slight rise recorded in the 3 kHz response can be explained by the incoming tide and the fact that signals at the lowest frequency penetrate the deepest depths. Note that the survey location was atop the earthen abutment of the tidal channel (see Fig. 2.2 A). A second possibility could be, that when the batteries were changed in between the two data sets, the profiler instrument went out of calibration and measured a higher apparent conductivity. A third explanation could be the effect of temperature on the profiler causing the resulting measurements to drift. The data set was collected in the afternoon on a sunny day, the profiler had been lying on the ground in direct sunlight all day, dramatically increasing its temperature. As the temperature of the profiler increases, it causes a drift in apparent conductivity readings. An example of this can be seen in Fig.4.1, which was taken from a study conducted in College Station by Mark Everett (pers. comm).

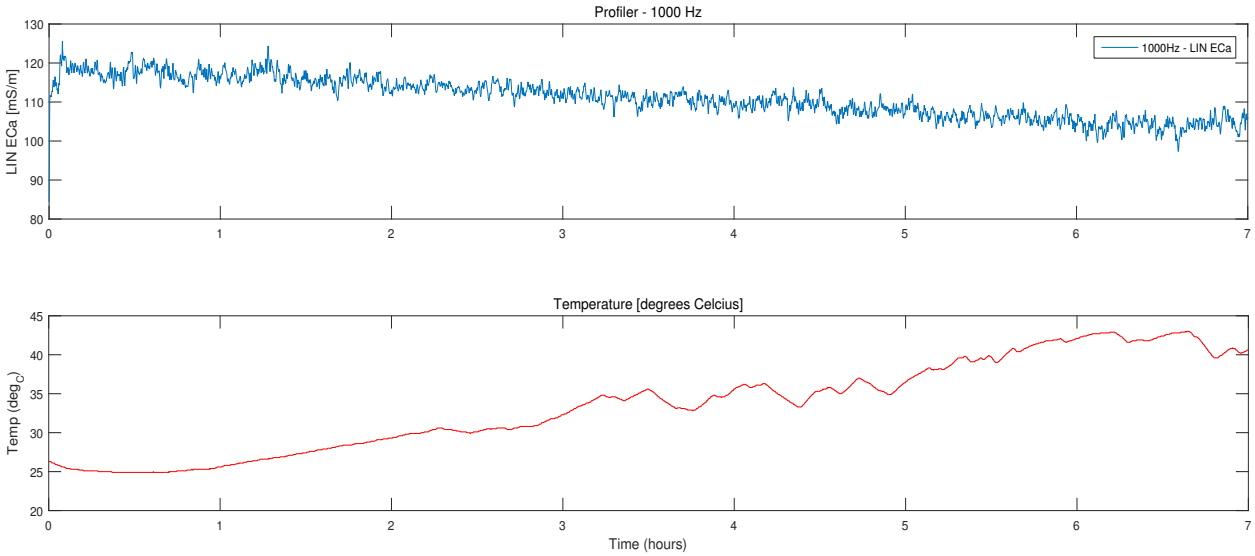

***Figure 4.1**: Graph relating Profiler downward drift of Apparent Conductivity measurements to temperature increase (pers. comm.).*

Such a thermal drift would explain the slight decrease in apparent conductivity at the two higher frequencies (10 & 15 kHz), while the 3 kHz response could have increased due to the rising tide, with that effect being large enough to overcome the trend of the opposite sign caused by temperature change of the profiler.

We did not observe a similar effect at the Sargent beach location. These data were collected on a cloudy day so the profiler did not heat up as much due to direct sunlight; also, the profiler was collected directly on the beach surface so that the instrument was closer to the putative groundwater table than was the case at the bridge abutment.

The time-series data at the Matagorda site, was collected during a falling tide. The first half of the readings, at all three frequencies, remains relatively constant, while the second half shows a slight rise in apparent conductivity measurements (~10 mS/m) at all three frequencies.

The absence of significant variations in apparent conductivity might be due to the location of the profiler relative to the waterline. The profiler was placed farther back (~35m) on the beach face and not close to the edge of the water, as was done at the Sargent beach location. A possible explanation for the subtle rise in apparent conductivity during the second half of the data acquisition might be the time lag of the tidal signature in the groundwater. Incoming flow of saline groundwater from the rising tide would be delayed, which could provide a reason for the rise in apparent conductivity even though the measurements were recorded during a falling tide. The spike in the middle of the plot is an anomaly caused when the batteries were changed, to avoid loosing any data, and should not be taken into consideration.

At the Sargent saltmarsh site, the spatial profiles were divided into sections consisting of individual levees (Fig. 4.2).

***Figure 4.2**: Divisions of spatial profile paths for Sargent, TX saltmarsh. The red path shows the route for the spatial profile referred to as "Main road to gate, south levee, and back". The purple path shows the route for the spatial profile referred to as "Main road, across bridge and back". The blue path shows the route for the spatial profile referred to as "North levee and back" (Google Earth).*

The segmentation is done in order to obtain high resolution data sets with out an excessively large file size. The spatial profiles reveal apparent conductivity variations across the study area, and were gathered on Jan. 19, 2017 during a rising tide. The spikes in apparent conductivity measurements for the spatial profile labeled red in Fig. 4.2 are anomalies caused by walking too close to, or over a steel pipeline on the ground and should not be considered hydrogeologically significant. For the spatial profile labeled purple in Fig. 4.2, the spikes were caused by walking across the bridge over the tidal inlet. These spikes are also considered to be anomalies without hydrogeological significance. The spatial profiles at the Matagorda location were divided into two data files, one for the walk down a given path, and the second for the walk back along the same path. The spike at the end of the spatial profile, i.e. at the end of the return trip, was caused by a passing truck while measurements were being recorded. This anomaly also should not be considered to have hydrogeological significance.

The repeatability graphs test the ability of the profiler to measure consistent EMI responses across a specified area. These tests were only done for the spatial profile data. The results (Figs. 4.4-4.7 & A-14 - A-24) show that the repeat measurements varied by substantial amounts at each location and frequency. An explanation for this could be the elapsed time between the first and second measurements along a certain path. The more time that passes between equivalent measurements, the greater is the potential for the tide-induced changes to have an impact on the measured apparent conductivity measured. Also, the route walked and location of the measurements was difficult to keep precisely the same. There will be some variation in the exact geographical coordinates for the first and second measurements. While only a minor change in position is expected, the potential for it to affect the measurements is present. A third explanation for variations in the repeatability graphs is the pace at which each

route was walked. Maintaining the same walking pace was attempted, but this is always an issue with conducting experiments with continuous, as opposed to discrete, data sampling.

Repeatability at the Sargent saltmarsh location was analyzed for each levee separately (Fig. 4.3).

Figure 4.3*: Paths for repeatability plots based on spatial profile paths for Sargent, TX saltmarsh. The red path shows the area for the repeatability graph referred to as "Main road to gate and back". The yellow path shows the area for the repeatability graph referred to as "South levee and back". The blue path shows the area for the repeatability graph referred to as "North levee and back". The purple path shows the area for the repeatability graph referred to as "Main road across bridge and back" (Google Earth).*

Three repeatability graphs that reveal good, average, and poor repeatability are shown here as examples, the remaining repeatability graphs can be found in the Appendix. The measurements gathered walking down the main road across the bridge and back (purple in Fig. 4.3) for the 3 kHz response produced a repeatability graph with the highest consistency (Fig. 4.4).

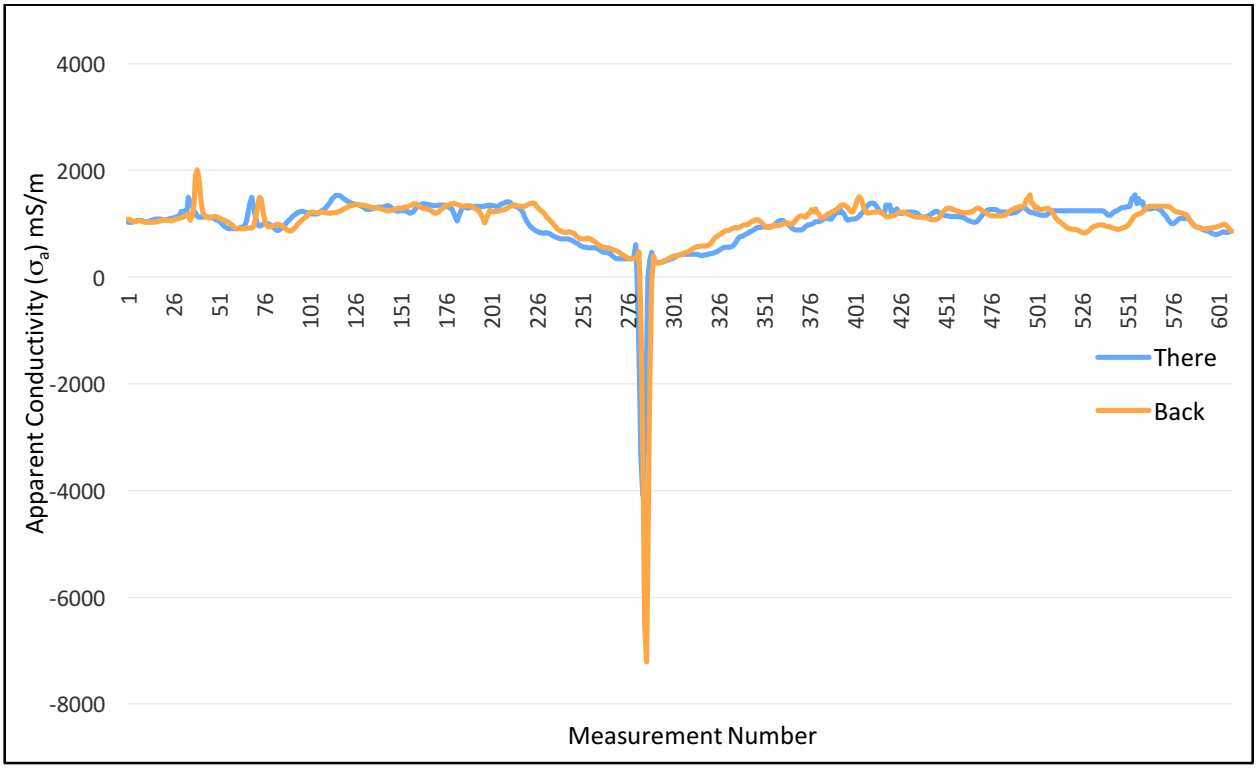

***Figure 4.4**: Repeatability graph (3 kHz) for Sargent, TX saltmarsh. Down main road, across bridge and back (purple path in Fig. 4.3).*

This graph shows similar apparent conductivity readings across the profile, with a few subtle shifts in the spike locations. The most likely rationale for these shifts would be a slight change in walking pace. This repeatability graph was also plotted in a different manner, plotting the apparent conductivity values against distance between the GPS coordinates (Fig. 4.5).

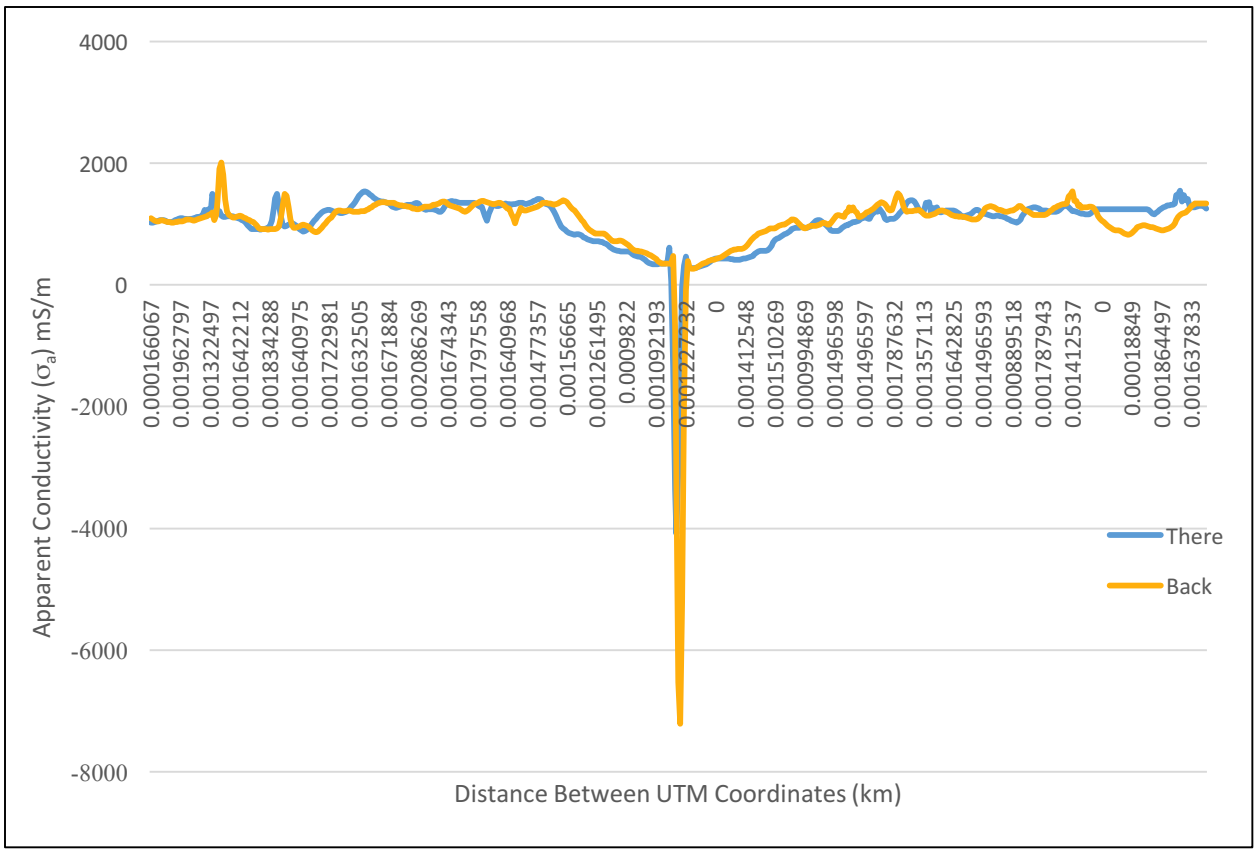

***Figure 4.5**: Repeatability graph (3 kHz) for Sargent, TX saltmarsh. Down main road, across bridge and back (purple path in Fig. 4.3) plotted against distance between GPS coordinates.*

This was done by converting the Lat/Long coordinates into UTM and finding the distance between to consecutive points. Plotting the spatial profiles or repeatability graphs against distance between coordinates, rather than measurement number, gives a better representation of the location the measurement was taken and helps show higher repeatability. The path down the north levee and back (blue in Fig. 4.3) shows a repeatability graph of average quality for the 15 kHz response (Fig. 4.6).

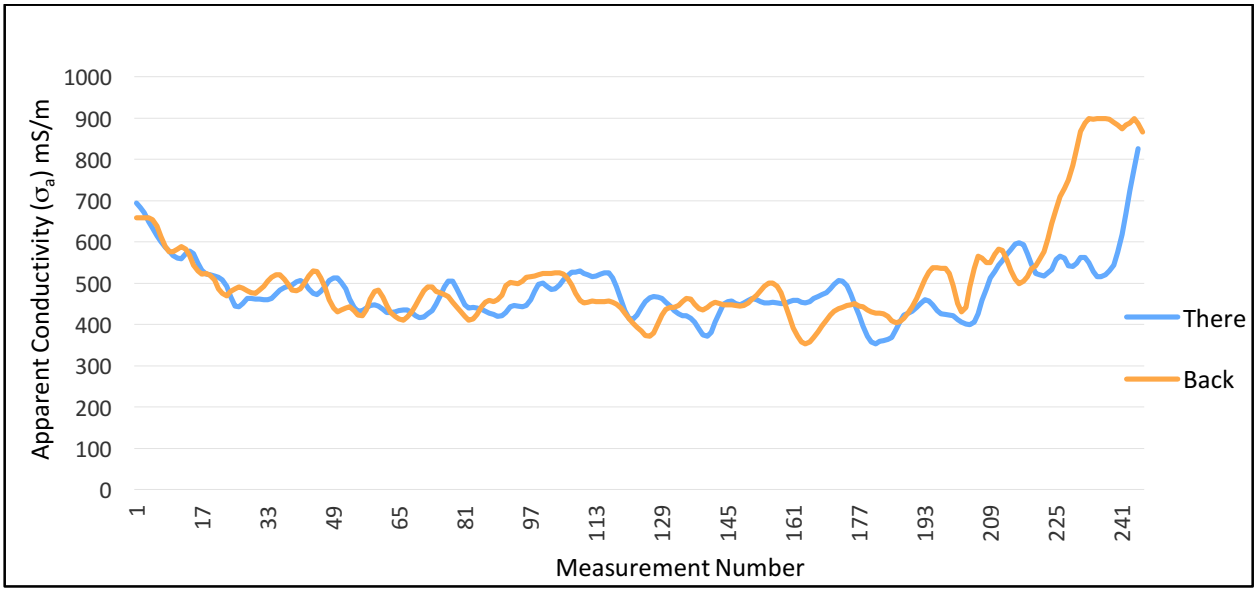

***Figure 4.6**: Repeatability graph (15 kHz) for Sargent, TX saltmarsh. Down north levee and back (blue path in Fig. 4.3).*

This graph shows some consistency in the general profile and shape of the measurements, but has some shifts and variations in measurements, which again are most likely due to a change in walking pace. Figure (4.7) shows the graph that exhibits the lowest repeatability, it was recorded for the path down the main road to the gate and back (red in Fig. 4.3) at 15 kHz frequency.

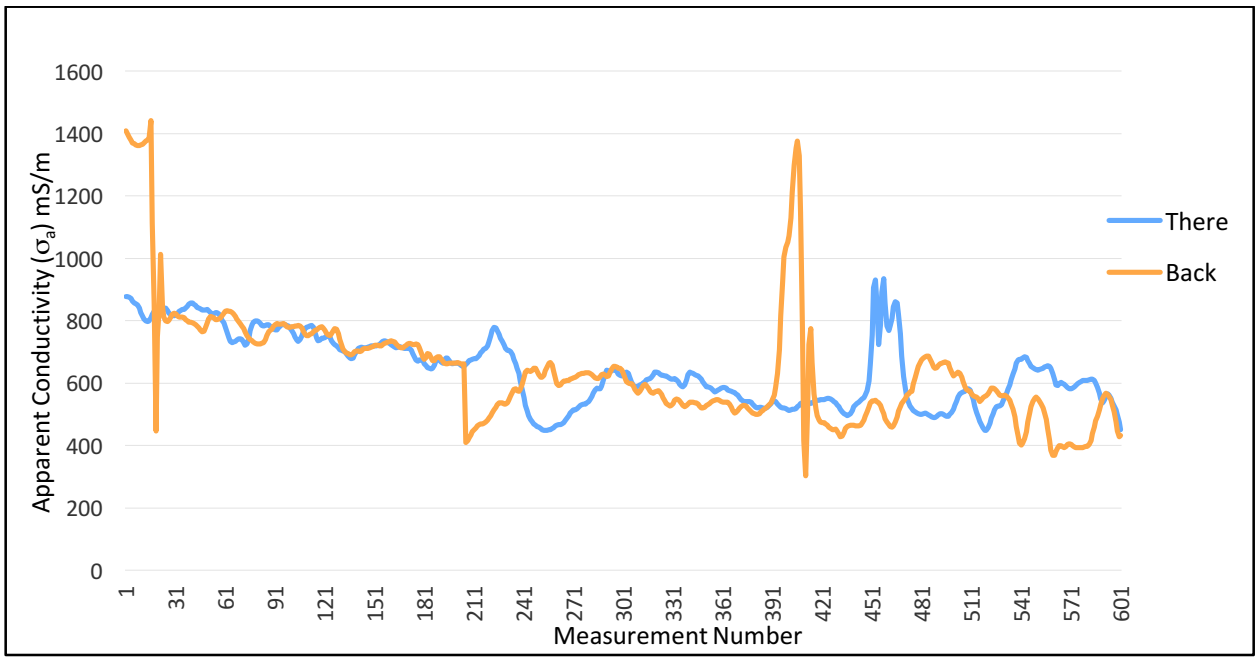

***Figure 4.7**: Repeatability graph (3 kHz) for Sargent, TX saltmarsh. Down main road to gate and back (red in Fig. 4.3).*

Possible explanations for the poor correlation between the two measurements could be a change in walking pace as well as a slight change in the measurement location. This path has several pipelines lying alongside it, so it is possible that, during the return trip, measurements were recorded closer to one of these pipelines than during the outbound measurements. This change in proximity of the sensor to the pipelines could easily cause the spikes seen in the graph.

The repeatability graphs for Matagorda do not show the same values for the two sets of measurements, outbound and inbound along the same path, but have the same profile shape offset by a roughly constant amount, i.e. there is a "DC bias" in the data. The DC offset could be due to the approx. one-hour gap between the two sets of measurements. Figure (4.8) shows the repeatability graph for the 3 kHz response.

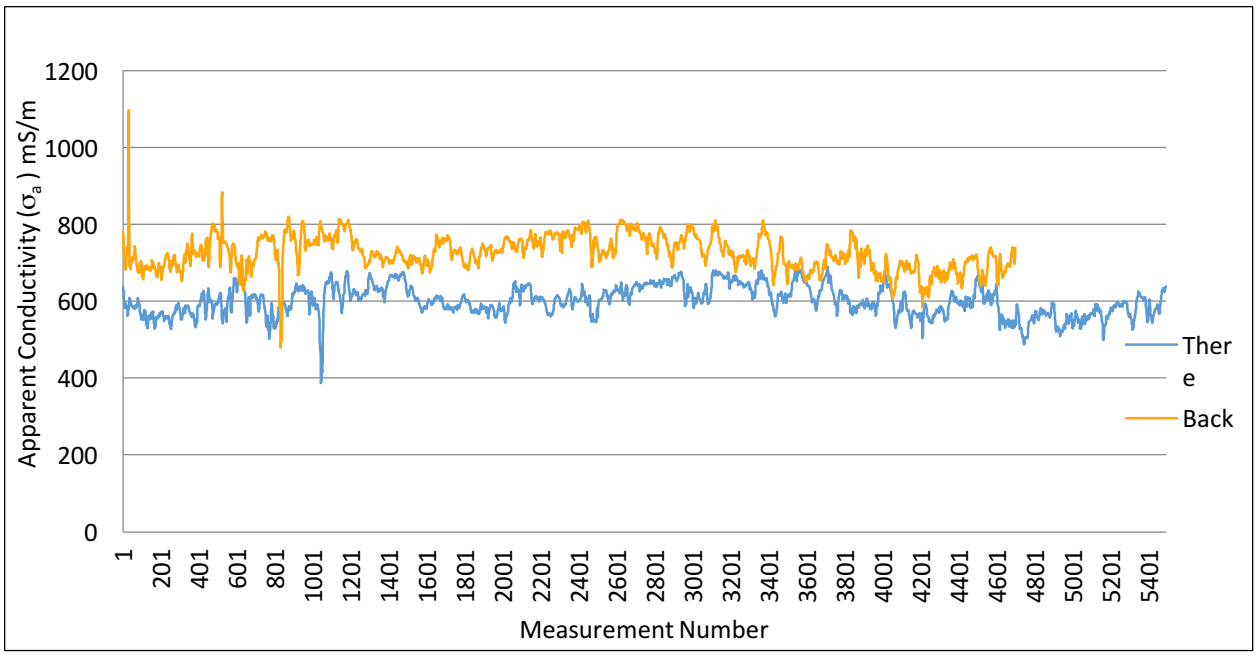

***Figure 4.8**: Repeatability graph (3 kHz) for Matagorda Peninsula (path shown in Fig. 3.3).*

The path walked to collect this data is shown in Fig. 3.3. This repeatability graph was also plotted in an additional manner, by plotting the apparent conductivity against the distance between GPS coordinates (Fig. 4.9).

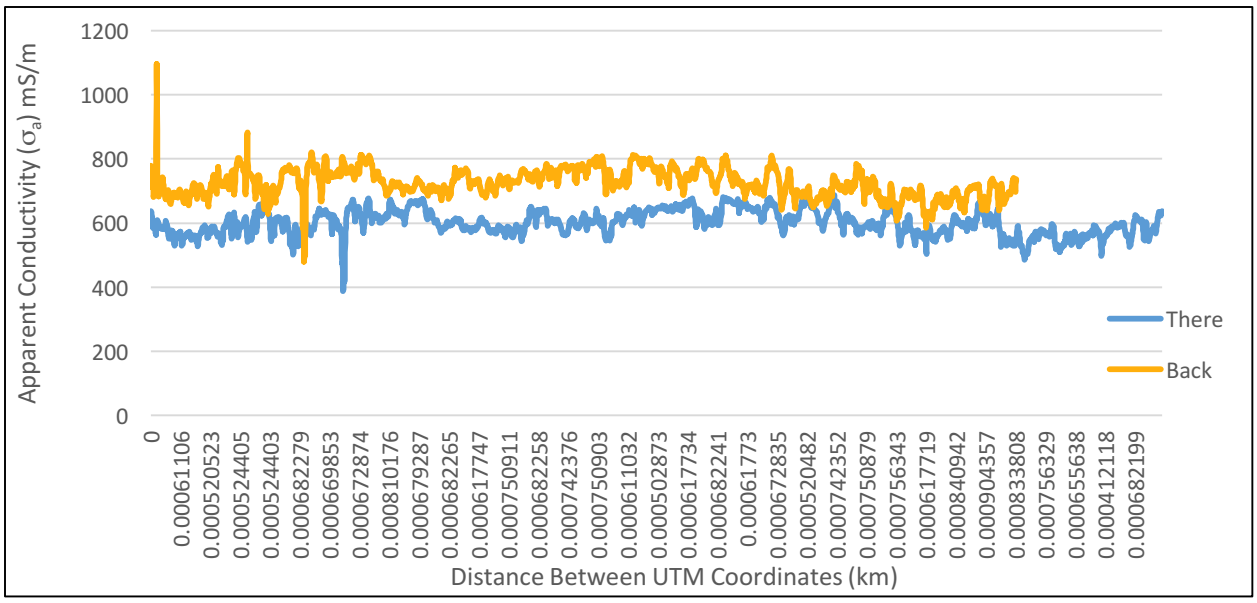

***Figure 4.9**: Repeatability graph (3 kHz) for Matagorda Peninsula (path shown in Fig. 3.3) plotted against distance between GPS coordinates.*

As shown in Fig. 4.8, the difference in apparent conductivity between the outbound and inbound measurements is ~100 mS/m. The hour-long time gap is considered to be the probable reason for this increase in apparent conductivity since the data were collected during a rising tide. As the time passed, presumably the saline groundwater level rose with the tide. Along with the increase in apparent conductivity values, it is apparent that from the difference in total number of data points acquired that the walking pace for the second measurements was faster, leading to fewer measurements being recorded on the inbound journey. The repeatability graphs for the responses at the other two frequencies can be found in the Appendix.

4.2 Fourier & Fractal Analysis

Fourier analysis represents continuous functions or discrete sequences of data using sums of simple trigonometric (sine and cosine) functions. Continuous Fourier transforms (FT) are used in mathematics to analyze the amplitude vs. frequency characteristics of continuous functions.

For the discretely sampled data that is typically observed in practice, Fourier analysis is done by applying a discrete Fourier transform (DFT). A continuous Fourier transform is a conversion of a function of time into a function of frequency (Francese, 2012), where the transform is defined by:

$$F(\omega) = \int_{-\infty}^{\infty} f(t) \exp(-2\pi i \omega t)\, dt$$

In the above formula, F(ω) is the Fourier transform, *t* is the time, and ω is the frequency (Oppenheim and Schafer, 2010). A FT converts a waveform *f(t)* into a number of sinusoids each having a complex amplitude F(ω). If the time function *f(t)* is discretely sampled, a discrete Fourier transform (DFT) is appropriate (Francese, 2012). The DFT is defined by:

$$A_n = A(\omega_n) = \frac{1}{N} \sum_{k=0}^{N-1} a_k \exp\,(-i\omega_n k \Delta t)$$

Where $\omega_n = {}^{2\pi n}/_{N\Delta t}$, $i = \sqrt{-1}$, *n* is the sample number (*n= 0, 1, 2,… N-1)* , and N is the total number of time samples (Everett, 2013). The quantity A_n is the complex coefficient associated with frequency ω_n.

An additional benefit to using a Fourier analysis is that it enables the computation of the power spectral density $|A(f)|^2$, which specifies the power in the signal *f(t)* at different frequencies (Eke et al., 2000). The estimated power spectral density is further useful in conducting a fractal analysis. In such an analysis, the power spectral density (PSD) function takes on a power-law form if the original signal exhibits certain fractal-like characteristics such as long-range-dependence (Everett and Weiss, 2002).

Fractal analysis is a special mathematical property of geometric objects that have the capability to describe patters containing spatial heterogeneities that span a wide range of scales. Fractals develop in space or time by the repeated operation of a process that results in objects or events that are characterized by self-similarity. The later refers to the apparent geometrical or

statistical similarity between elements of the object or event independent of the scale of observation (Eke et al., 2000). In other words, an object is said to be fractal if there is self-similarity, or relatively the same pattern can be seen regardless of the scale. An object that exhibits length-dependent heterogeneity, i.e. it is heterogeneous at different scales but the patter may be different at each scale, can be said to be "fractal-like" but not self-similar.

Apparent conductivity measurements, detected by electromagnetic induction responses, typically show characteristics of fractional Brownian motion (fBm), a class of non-stationary signals that describe processes with long-range correlations (Everett and Weiss, 2002). After plotting apparent conductivity measurements, observing the profile, and conducting Fourier analysis to get the amplitude, a fractal analysis can be conducted through evaluation of the PSD function. The amplitude produced through Fourier analysis is useful for determining whether the PSD has the shape of a power-law of the form $|A(f)|^2 \sim f^{\beta}$, where A is the amplitude and β is the slope when the function is plotted on log-log axes (Everett and Weiss, 2002). If the power spectrum has a power law shape, then the original signal is a fractal-like signal.

From my study, both Fourier and fractal analyses were conducted in Excel. In order to determine if a signal can be characterized as fractal-like, a Fourier analysis must be done first. A Fourier analysis was run on every 3 kHz apparent conductivity spatial profile. Using the "Fourier Analysis" tool in Excel on the apparent conductivity measurements produces an array of complex numbers. The length of the complex array is the same as that of the number of measurements, although only the first half of the array needs to be used since the second half contains redundant information. Each element of the array corresponds to the contribution to the original signal of a sinusoid characterized by a specific wavenumber. A wavenumber is the inverse of wavelength and may be thought of as a "spatial frequency." Once this was done, using

the “IMREAL” and “IMAGINARY” functions gives the real and imaginary components of the complex numbers in the array. Squaring the real and imaginary components then adding them together produces the squared-amplitude value for each wavenumber. Plotting these amplitude values against the wavenumber (equivalently, the measurement number, since the wavenumbers are evenly spaced) on a log-log plot yields the PSD of the original signal. In order to test if the signal is fractal, a best-fit line, or trendline, is fitted to the plot. If a trendline fits the data, i.e. the PSD is a power-law form, then the signal can be regarded as fractal-like. The slope $|\beta| > 1.0$ of a fitted trendline is characteristic of fractional Brownian motion (Everett and Weiss, 2002).

Fig. 4.8 shows the PSD, along with a best-fit power line, of the apparent conductivity profile recorded at the Sargent saltmarsh site (red in Fig. 4.2) for the 3 kHz frequency signal.

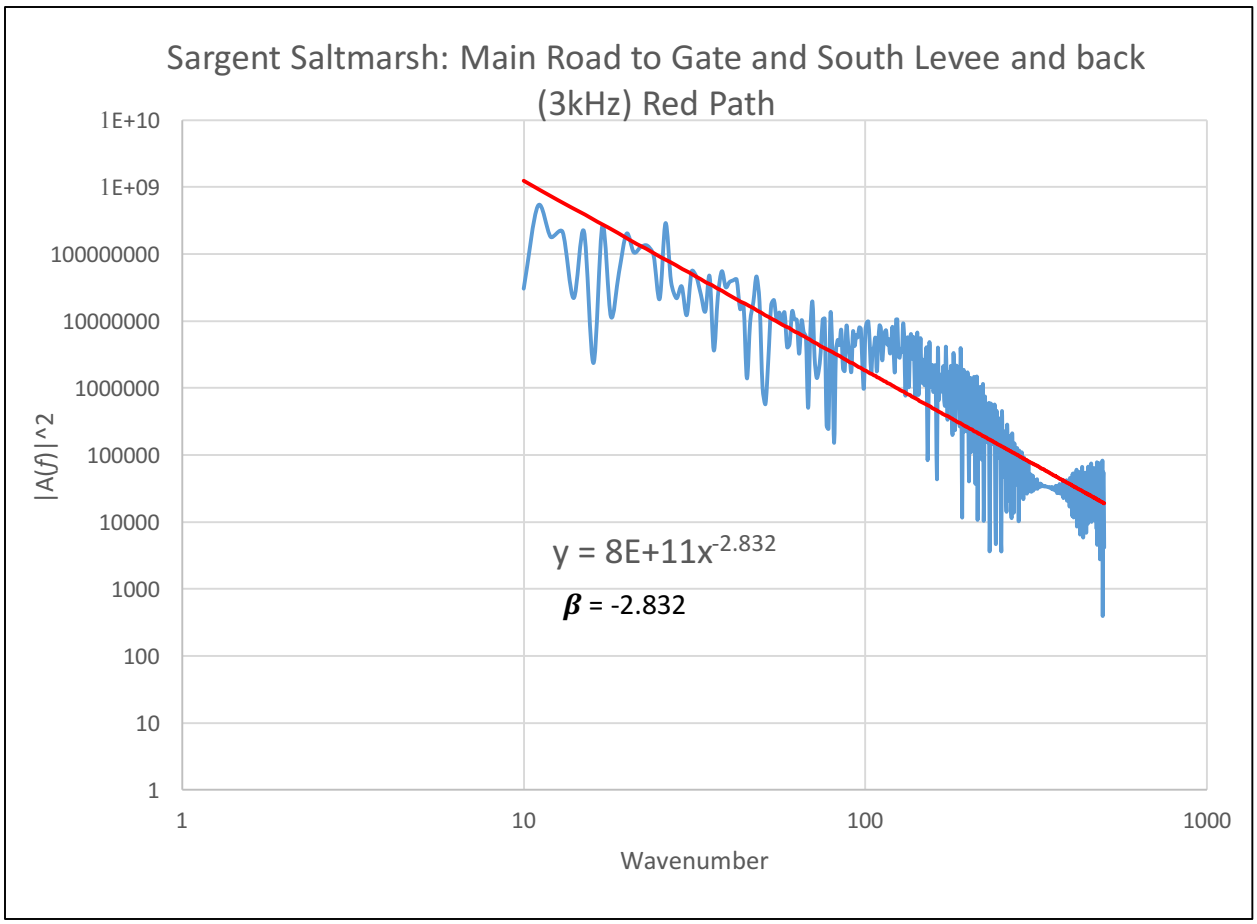

***Figure 4.10**: Power spectral density (PSD) of the apparent conductivity profile (3 kHz) in A- 9, along with a best-fit power line (red path in Fig.4.2).*

The equation for the best-fit power line with slope (β) is provided on the plot. The β value of -2.832 obeys $|A(f)|^2 \sim f^{\beta}$, and since$|\beta| > 1$ the signal is fractal-like and characterized as fBm. Fig. 4.9 shows the PSD, along with a best-fit power line, of the apparent conductivity profile recorded at the Matagorda location (Fig. 3.3) for the measurements heading in one direction (outbound) for the 3 kHz frequency signal.

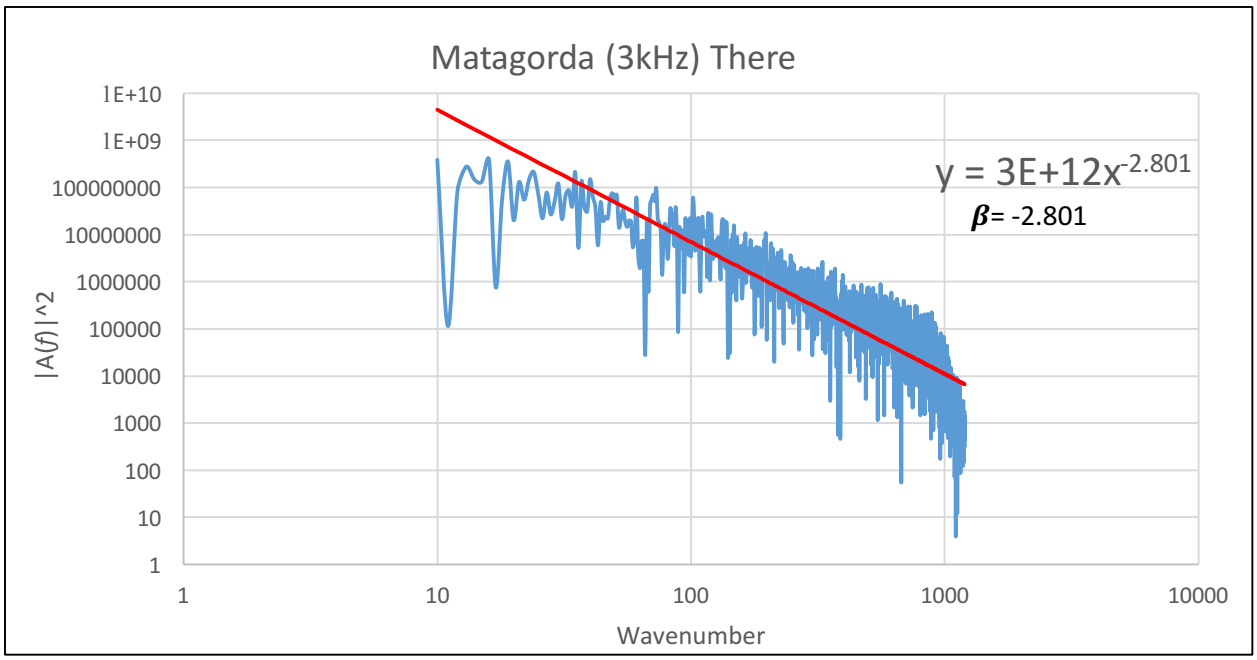

***Figure 4.11**: Power spectral density (PSD) of the apparent conductivity profile (3 kHz) in A-12, along with a best-fit power line.*

The β value of -2.801 also obeys $|A(f)|^2 \sim f^{\beta}$ with $|\beta| > 1$, characterizing this signal also as fBm. The PSD slope β provides an effective measure of length-dependent spatial heterogeneity. As the slope steepens, the signal is influenced by long-range (i.e. small wavenumber) correlations and less by small-scale fluctuations (i.e. large wavenumber) (Everett and Weiss, 2002). Considering this, after looking at the two slopes, the Sargent saltmarsh location with its larger |β| appears to have slightly more small-scale heterogeneity in the subsurface than does the Matagorda location. While the differences in slopes is small, it could be related to the higher mud content at Sargent, with its more tortuous pore geometry than would be expected at a sand-dominated environment such as Matagorda.

4.3 Implementation of Wavelet Analysis

The data for the spatial profiles were further analyzed through a statistical software environment called RStudio. This is an integrated development environment for the well-known

statistical package, R [see www.r-project.org]. R is a free software environment for statistical computing, data manipulation, and graphics, that runs on a variety of UNIX platforms and similar systems such as Windows and MacOs. Essentially, RStudio is a wrapper, or more user-friendly environment, that can be used to perform all the statistical analysis functions of R. Data sets are easily transferred into or read by RStudio, and from there a large variety of different computing, manipulation, and graphics processes can be executed depending on the scope of the study at hand. For the present study, wavelet analysis was performed using the R software package.

4.4 Wavelet Analysis

Wavelet analysis is a pictorial way of analyzing spatial data by observing how the wavenumber content of a signal varies along a profile. By decomposing a spatial series into position-wavenumber space, one is able to determine both the dominant modes of variability and how those modes vary along the profile (Torrence and Compo, 1998). The equivalent time-domain concept is a decomposition into time-frequency space. Wavelet analysis deals with expansion of the sampled data in terms of a set of basis functions, like Fourier analysis. Unlike Fourier analysis, wavelet analysis expands sampled data not in terms of trigonometric polynomials but in terms of wavelets, which are generated in the form of translations and dilations of a fixed function called the mother wavelet (Lee and Yamamoto, 1994). Here, discrete wavelet transform (DWT) analysis is used, because discrete data samples were collected, as opposed to a continuous function. Lee and Yamamoto (1994) define a discretized wavelet in the time domain as:

$$\psi_{m,n}(t)\ a_0^{-\frac{m}{2}}\psi\left(\frac{t-nb_0}{a_0^m}\right)$$

where ψ is the mother wavelet, a and b are the scale and shift parameters, and m and n are integer values. The discrete wavelet transform is defined as:

$$S_{m,n} = \int_{-\infty}^{\infty} \psi'_{m,n}(t)s(t)dt$$

where the function $\psi_{m,n}(t)$ provides sampling points on the scale-time plane (Lee and Yamamoto, 1994).

Using the wavelet transform function in RStudio, called "wt()" [see www.r-project.org], produces a 2-D plot showing how the dominant EMI signal wavelength changes along the spatial profile, for each of the three TX operating frequencies. Wavelet analysis was only conducted on the spatial profile data. This is because there is greater variability in the measurement variations along the spatial profile (the spatial data are non-stationary, that is, the mean and variance change along the profile), whereas the time-series data appear to be stationary, that is, the mean and variance are constant throughout the measurement interval, apart from a linear trend in some cases. When examining a wavelet plot, a main takeaway is that if the measurement variations are compact, or restricted to a certain small sub-interval of space, the signal will be spread out across a broad swath of wavelengths. Conversely, if the measurement variations are spread out in space the signal power will have a single dominant wavelength. The equivalent statements in the time domain are that an impulse is a broadband signal where a perfect sinusoid is narrow-band, actually it is a spike in the frequency domain.

Two examples of wavelet plots and their analysis are presented. The first wavelet plot (Fig. 4.12) was produced from the spatial profile marked red in Fig. 4.2 for the 3 kHz signal.

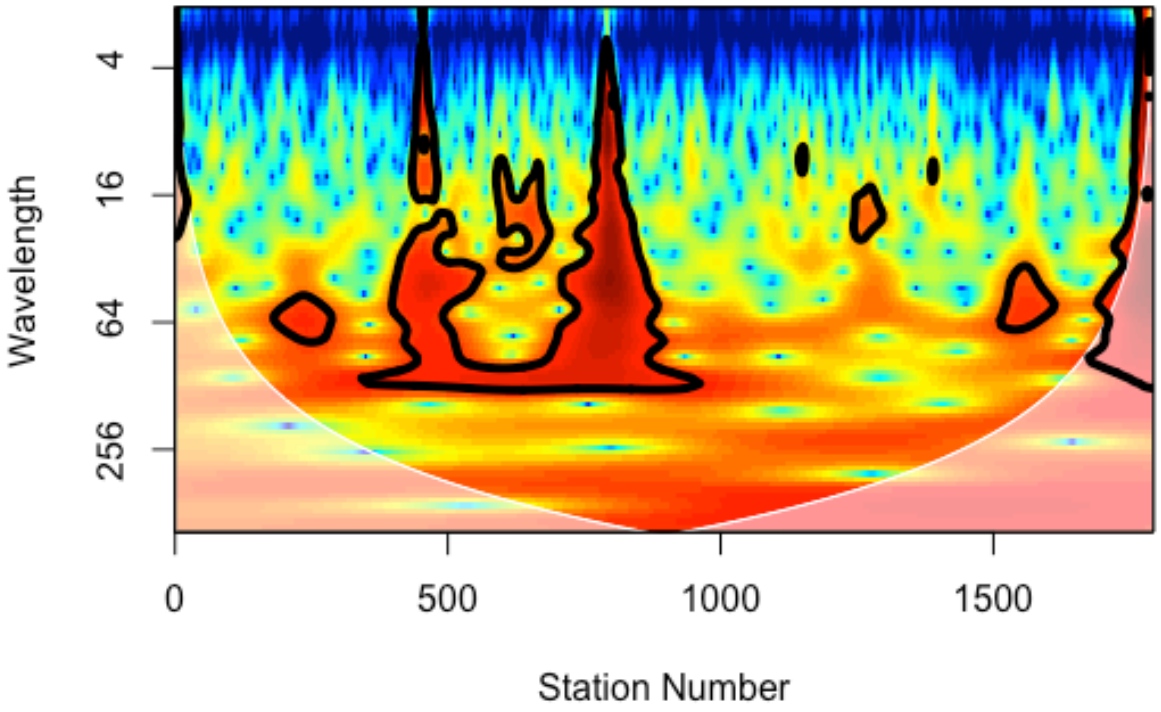

***Figure 4.12**: Wavelet plot for Sargent saltmarsh, spatial profile (3kHz) marked red in Fig. 4.2; showing the power in signal wavelength at given locations along the profile.*

The spatial profile can be found in A-9. Upon examination of the wavelet plot and the spatial profile, it is evident that the two main spikes in the spatial profile appear on the wavelet plot as vertically elongated blobs. The spike seen in the spatial profile is likely a response caused by a pipe and, accordingly it is compact in space. However, the associated blob seen in the wavelet plot is tall and elongated, this is because the power from the pipe signal is spread out across a broad swath of wavelengths. Generally, the blobs can be related to spikes, bursts, or "bays" (an excursion of a data series from its overall mean that extends over a significant number of measurements) in the spatial profile. The the remainder of the profile, not characterized by spikes, bursts, or bays, appears mainly as noise on the wavelet plot, not defined by a blob. The

colors on this plot can be interpreted as signal power, with the dark red indicating a higher amplitude signal power and blue indicating the lowest signal power. The next example (Fig. 4.13) is the wavelet plot for the 3 kHz measurements recorded along the spatial profile for Matagorda (Fig. 3.3) going in one direction only, it does not include the second set of measurements recorded with the operator heading in the opposite direction.

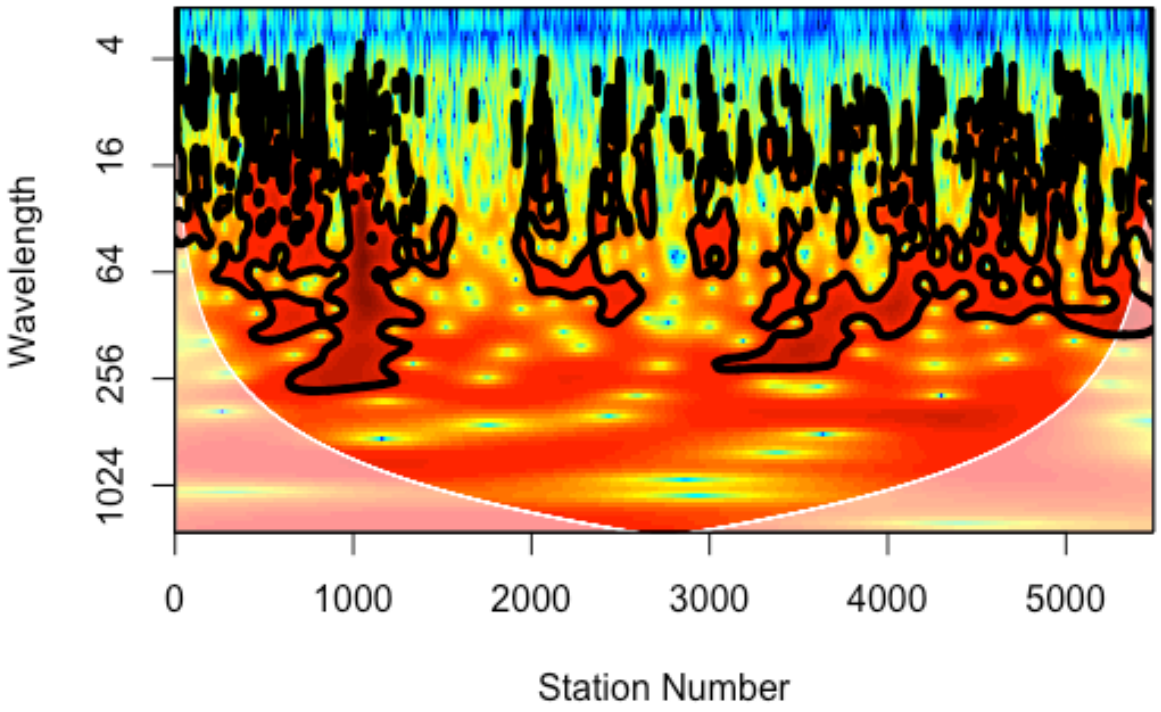

***Figure 4.13**: Wavelet plot of Matagorda spatial profile (3kHz) measurements taken along the profile in one direction ("There"), shown in Fig.3.3; showing the power in signal wavelength at given locations along the profile.*

The wavelet plot is complex and chaotic showing multiple elongated blobs spread out over all wavelengths. Upon examining the plot, the Matagorda data series can be classified as having

broadband, or spikey, structure in the spatial domain. In effect, there are many signals of different wavelengths riding on top of each other, that is, there are multiple different wavelengths embedded across the profile. In other words, there is not one particular dominant wavelength. Wavelet analysis is a useful tool if one or more dominant wavelengths are evident across the profile. A wavelet analysis of the Matagorda spatial profile therefore may not be the most useful form of analysis due to its broadband structure and the many differing signals and wavelengths that seem to contribute to the data throughout the profile.

5. DISCUSSION

Recently, EMI methods have been used to analyze different aspects of coastal systems for various purposes (Sejimonsbergen et al., 2004; Vrbancich, 2009; Christensen and Halkjaer, 2010; Nenna et al., 2013; Delefortrie et al., 2014; Weymer et al., 2016). This study describes how EMI geophysical surveys can be used to examine the subsurface components of coastal systems including tidal-influenced groundwater, using various ways to analyze the data, and comparing results with those found in a previous study along the Texas coast (Weymer et al., 2016) in addition to EMI studies in other geological settings using similar analysis techniques (Everett and Weiss, 2002; Beskardes et al., 2017). Weymer et al. (2016) examined how groundwater flow induced by tidal fluctuations influence apparent conductivity measurements, complicating interpretations of deeper geologic framework. While Everett and Weiss (2002) and Beskardes et al. (2017) describe some of the analysis techniques used in the current study, these techniques are conducted and interpreted for different geological settings; for example, a floodplain and a fractured sandstone aquifer. Fluctuations in subsurface apparent conductivity are expected to result from spatiotemporal variations in the exchange of fresh and saltwater in response to rising and falling tides over a tidal cycle. Nielsen (1990) suggests that there should be a tide-dependent step response in the sub-beach saline groundwater level over a 12-hour tidal cycle; Weymer et al. (2016) saw evidence for this in σ_a measurements. Nielsen (1990) examined the influence of tidal cycles on the fluctuation and position of the water table beneath a sandy beach using monitoring wells and observed 3 main characteristics: 1) the minimum water level is significantly higher than the low tide level; 2) despite the roughly sinusoidal nature of the tidal

cycle, the temporal variation in the water table is not sinusoidal but more characteristic of a step-like function; 3) the maximum water level was a few cm higher than the high tide level.

In a similar study to the current one, Weymer et al. (2016) obtained time-series data at a fixed location and a spatial profile of a sandy beach at Padre Island National Seashore (PAIS), by collecting σ_a measurements using the same profiler instrument as used in this study. Weymer et al. (2016) collected time-series data over a 12-hour period and multiple spatial profiles along the same transect between November 2013 and March 2015. The spatial profiles were collected across such a wide range of time (several months) in order to examine possible seasonality variations in apparent conductivity readings. Although the tidal signal displays a periodic trend, the EMI time-series signal follows a step-function-like pattern. The results for the time-series data described by Weymer et al. (2016) are as follows; at low tide the σ_a values remained fairly constant for 4 hours and then suddenly jumped, with the timing of the jump preceding high tide by nearly 3 hours, and then remained consistently high for up to 3 hours after high tide and then suddenly dropped off. In summary, the EMI responses exhibited a lead/lag step-response that increases rapidly preceding high tide then drops off slowly during falling tide.

In the current study, the time-series data collected for the Sargent saltmarsh site (see A-7) are comparable to the measurements made at PAIS. The first segment of data does not display any significant variation of apparent conductivity; however, the second data set, marked by the spike on the graph, shows a jump in apparent conductivity. These measurements were recorded over a time from ~3:00-5:00 p.m., where there was a jump in apparent conductivity by ~90 mS/m in the 3 kHz signal and ~70 mS/m in the 10 kHz and 15 kHz signals, with high tide at 9:30 p.m. This increase in σ_a was observed ~6 hours before high tide, whereas Weymer at al. (2016) observed the jump 3 hours before high tide. While this comparison to the findings by Weymer et

al. (2016) cannot be made with certainty due to the lost key data set, it is still important to note the jump in apparent conductivity across all three frequencies. The spatial profile for the Matagorda location (see A-23 & A-24) shows some similarity to the results found by Weymer et al. (2016). The measurements were recorded twice, one from ~10:30am-12:00 p.m., and the second from ~1:00-2:15 p.m. On the day of data collection, high tide was at 5:00 p.m. An increase in apparent conductivity of ~100 mS/m was observed, and occurred roughly 4 hours before high tide, which is relatively consistent with the findings of Weymer et al. (2016). The remaining time-series data for the Sargent beach and Matagorda locations are not consistent with the results from Sargent saltmarsh, the variation in measurements for the Matagorda spatial profile, or those found by Weymer et al. (2016). This is likely due to lost data files and the brief time period in which the measurements were recorded. The data does not span an entire tidal cycle, but rather only a small segment of it, so definitive conclusions and correlations to Weymer et al. (2016) cannot be drawn.

The spatial data analysis techniques presented in the current study are similar to those used in two previous studies (Everett and Weiss, 2002; Beskardes et al., 2017). The two previous studies used Fourier Transform and PSD to determine the power of an EMI signal data series as a function of wavenumber. This is done to determine whether the EMI signal is fractal-like, as a way of examining the roughness of an EMI signal, and ultimately to relate it to the heterogeneity of the subsurface. Everett and Weiss (2002) used EMI data to study two areas characterized by different geology, a floodplain alluvium in Brazos County and a fractured sandstone formation in Mason County. The analysis was performed by collecting apparent conductivity measurements. For both locations apparent conductivity profiles were created to observe how σ_a varied along a spatial profile. Then the PSD was examined as a more quantitative approach to determine if the

signal is fractal-like and could be characterized as fBm or Gaussian noise. After analyzing the PSD at both locations in the study, Everett and Weiss (2002) found that the floodplain generated a slope $\beta = -1.44$. At the Mason County area, two surveys were conducted with different intercoil spacing, 10 m and 20 m. The data using the 10 m intercoil spacing produced a slope $\beta = -2.08$ while the 20 m spacing produced a slope $\beta = -2.87$. All of these signals are classified as fBm, since a value of $|\beta| > 1$ indicates a non-stationary fractal-like signal (Everett and Weiss, 2002). Going into further detail, Everett and Weiss (2002) explained that the PSD slope β provides an effective measure of spatial heterogeneity in fractal signal; as the slope β steepens, the signal is influenced more by long-range correlations and less by small-scale fluctuations. The Mason County unit contains more dramatic long-range geological structure and stratigraphic contrasts than the heterogeneous floodplain in Brazos County (Everett and Weiss, 2002). Beskardes et al. (2017) did a similar study in Mason County but examined apparent conductivity and PSD over several different lithologies: granite, marble, sandstone, and maroon soil. After examining the PSD for all the geological units, slope β values ranging from -1.699 – -2.697 were found, characterizing all signals as fBm. Beskardes et al. (2017) presented a computational method to generate synthetic EMI responses that are characterized by dependencies over short, medium, and long-range scale. That is, fBm signals were synthesized. The resulting models focused mainly on horizontal spatial correlation of geologic textures but do not take account of vertical geological stratification.

In the present study, apparent conductivity profiles were first obtained, then the PSD of each signal was analyzed using Fourier analysis. All signals found had a PSD slope $|\beta| > 1$, implying that every signal is fBm characterized by a fractal-like response, confirming the observations made by Everett and Weiss (2002) and Beskardes et al. (2017). While the slope

values varied between the two locations, with the mud-dominated Sargent site having a slightly higher β than the sand-dominated Matagorda site, this difference is not significant indicating that both locations have similar levels of heterogeneity.

While slope (β) values are dependent on the location of the area under investigation, they provide useful information about the underlying geology. The β value (-2.832) for the Sargent saltmarsh site, indicates that the signal has a higher power at smaller wavenumbers, and therefore is influenced more by long-range correlations than the β (-2.801) at Matagorda beach. The mud-dominated saltmarsh area contains more dramatic geologic structural and stratigraphic contrasts than the sand-dominated Matagorda beach. The signal at Matagorda beach can be characterized as having smaller wavelengths and influenced more by larger wavenumbers. Thus, larger-scale electrical apparent conductivity variations in the subsurface are expected to be more pronounced at the Sargent saltmarsh, which is observed in my results by the steeper PSD slope recorded. From this, the sand-dominated Matagorda beach can be said to have less heterogeneity in the subsurface than that of the Sargent saltmarsh, which could potentially be attributed to the high mud content, the engineered levees, pipelines, and other possible subsurface features such as sand and clay lenses.

As shown in this study, there are several techniques to analyze EMI signals and each technique gives slightly different information about the subsurface. The analysis methods producing the highest quality quantitative information may vary between study locations based on prevailing geological, geophysical, and hydrological properties; however, analyzing data using multiple different methods is suggested in order to produce the most accurate interpretation.

6. CONCLUSION

Dynamic and complex, coastal systems have been studied in numerous geological and geophysical contexts including hydrological, environmental, and engineering site evaluations. Enabling non-invasive investigations of the subsurface component, geophysical methods and instruments have been widely used to examine these coastal systems. My thesis describes several methods of analyzing geophysical data, while investigating the tidal influence on hydrodynamics of coastal systems. I have examined temporal and spatial variations in EMI signals at two locations, Sargent and Matagorda on the Texas Gulf coast, and compared the results to those found in a previous similar study at Padre Island National Seashore.

Groundwater flow behaves in a different manner than surface water flow; the relationship between groundwater and the fluctuating tide was investigated by obtaining time-series and spatial profile electromagnetic geophysical data, using a portable multi-frequency EMI profiler, the GSSI Profiler EMP-400^{TM}. This relationship was examined by recording apparent conductivity measurements at three frequencies simultaneously; 3 kHz, 10 kHz, and 15 kHz. Once the data were collected they were first analyzed in Excel by plotting the apparent conductivity measurements against the measurement number. These data were then compared to the surface tidal charts obtained from NOAA to check for similarities. Time-series data were collected at two fixed locations at Sargent, at the beach and in the adjoining saltmarsh, and at one fixed location on the beach at nearby Matagorda peninsula. Spatial profiles were collected in the saltmarsh at Sargent (Fig. 3.2) and along the water line on the beach at Matagorda (Fig. 3.3); measurements were recorded at the same locations while traversing in both directions to test for

repeatability. The spatial profile data, for both locations, were analyzed using three additional methods; wavelet, Fourier, and fractal techniques.

Some of the data sets collected here are consistent with the previous findings of Weymer et al. (2016), namely the time-series data for the Sargent saltmarsh site and the spatial profile for the Matagorda site. Weymer et al. (2016) observed a lead/lag step-response in the apparent conductivity measurements, increasing rapidly preceding high tide by nearly 3 hours then dropping off slowly during falling tide. While comparable, the apparent conductivity measurements found in the current study did show an increase, but they preceded high tide by nearly 4 hours not 3. While obtaining data measurements, a fairly major but common issue arose. Several data files were lost while changing the batteries of either the profiler or PDA, causing them to be unrecoverable and either leaving gaps in the data or deleting the beginnings/ends of data series.

The most probable reasons for observing inconsistent results to Weymer et al. (2016), are the length of time data was collected and the missing data files. Here data were collected for only a short time, 2-4 hours at each location, which is a modest fraction of a tidal cycle; while Weymer et al. (2016) collected data over a time period of 12 hours, thereby observing EMI responses for an entire tidal cycle. If data were to have been collected over a longer length of time (~12 hours) and no data files were lost, it is possible that similar results would have been captured as those found at PAIS.

Analyzing geophysical data using multiple methods is always beneficial and encouraged, as each analysis method reveals different information leading to a more robust interpretation. Wavelet, Fourier, and fractal analysis were used to examine the spatial profiles in order to gain a better understanding of spatial variation in apparent conductivity. Wavelet analysis was

conducted because it offers a pictorial way of analyzing the data by decomposing a spatial-series into position-wavenumber space, determining the dominant wavelengths of variability (Torrence and Compo, 1998). While wavelet analysis provided useful information at the Sargent saltmarsh, unfortunately it was not the most effective analysis tool for the Matagorda beach because a broad swath of wavelengths characterized the EMI response throughout the profile. It did, however, allow the beach to be characterized as having broad band wavenumber structure, which implies abundant fine-scale spatial variations.

Through the use of Fourier and fractal analysis, it was determined that all the original measurement signals are fractal-like and can be classified as fractional Brownian motion (fBm) because the Fourier analysis revealed a power spectral density (PSD) function with a power-law shape. These findings agree with those found by both Everett and Weiss (2002) and Beskardes et al. (2017) in widely different geological settings.

Geophysical analysis of coastal systems can provide better understanding of the implications of groundwater dynamics during the tidal quiet-time response, with attendant implications for coastal management, ecological, and recreational purposes. My thesis serves as an example for how to utilize geophysical instrumentation, collect data, and employ various analysis techniques. I have interpreted my data with the motivation of learning more about how tidal fluctuations influence groundwater dynamics, and I have compared my results to those found in previous studies. It is recommended for future research that data be collected over a longer time frame (12 hours), multiple measurements should be made at the same location, a temperature logger should be carried while recording measurements, and caution should be used while using geophysical instruments, such as the profiler, so that no data are lost.

REFERENCES

Ataie-Ashtiani, B., R.E. Volker, and D.A. Lockington, 2001, Tidal Effects on Groundwater Dynamics in unconfined Aquifers: Hydrological Processes, **15**, 655-669.

Beskardes, G. D., C. J. Weiss, and M. E. Everett, 2017, Estimating the power-law distribution of Earth electrical conductivity from low-frequency, controlled-source electromagnetic responses: Geophysical Journal International, **208**, 639-651.

Callaghan, D.P., T.J. Bouma, P. Klaassen, D. van der Wal, M.J.F., Stive, and P.M.J., Herman, 2010, Hydrodynamic forcing on salt-marsh development:Distinguishing the relative importance of waves and tidal flows: Estuarine, Coastal and Shelf Science, **89**, 73-88.

Cartwright, N., Nielsen, P., 2001, Groundwater dynamics and salinity in beaches: Proceedings of Coasts and Ports 2001, 15th Australian Coastal and Ocean Engineering Conference, Gold Coast, Australia, 441-446.

Christensen, N.B., and M. Halkjaer, 2010, Mapping pollution and coastal hydrogeology with helicopter transient electromagnetic measurements: Exploration Geophysics, **45**, no. 4, 243-254.

Davidson-Amott, R., 2010, An introduction to coastal processes and geomorphology: Cambridge University Press, New York.

Delefortrie, S., T. Saey, E. Van De Vijver, P. De Smedt, T. Missiaen, I.Demerre, and M. Van Meirvenne, 2014, Frequency domain electromagnetic induction survey in the intertidal zone: limitations of low-induction-number and depth of exploration: Journal of Applied Geophysics, **100**, 14-22.

Eke, A., P. Herman, J. B. Bassingthwaighte, G. M. Raymond, D. B. Percival, M. Cannon, I. Balla, and C. Ikrenyi, 2000, Physiological time series: distinguishing fractal noises from motions, *Pflugers Arch.-Eur. J. Physiol*., no.439, 403-415.

Everett, M. E., and C. J. Weiss, 2002, Geological noise in near-surface electromagnetic induction data: Geophysical Research Letters, **29**, no. 1., 10-1 – 10-4.

Everett, M.E., and C. Farquharson, 2012, Near-surface electromagnetic induction- Introduction: Geophysics, **77**, no. 4, WB1-WB2.

Everett, M. E., 2013, Near-surface applied geophysics: Cambridge University Press, New York.

Francese, R. R., 2012, Spectral analysis of thinning beds using ground penetrating radar, Texas A&M University.

Geophysical Survey Systems, Incorporated. 2007, Profiler EMP-400 user's manual: Geophysical Survey Systems, Incorporated, User's Manual.

Haslett, S.K., 2009, Coastal Systems second edition: Routledge, New York.

Horn, D. P., 2002, Beach groundwater dynamics: Geomorphology, **48**, no.1, 121-146.

Horn, D. P., 2006, Measurements and modelling of beach groundwater flow in the swash-zone: a review: Continental Shelf Research, **26**, 622-652.

Huang, H. M., M. Deszcz-Pan, and B. Smith, 2008, Limitations of small EM sensors in resistive terrain, *in* 21st EEGS Symposium on the Application of Geophysics to Engineering and Environmental Problems, **21**, 163-180.

Lanyon, J.A., I.G. Eliot, and D.J. Clarke, 1982, Groundwater-level variation during semidiurnal spring tidal cycles on a sandy beach: Australian Journal of Freshwater Resources, **33**, 377-400.

Lee, D. T.I., and A. Yamamoto, 1994, Wavelet analysis: theory and applications: Hewlett-Packard Journal, **45**, 44-52.

McGowen, J. H., L. F. Brown, Jr., T. J. Evans, W. L. Fisher, and C. G. Groat, 1976, Environmental geologic atlas of the texas coastal zone- Bay City-Freeport area: University of Texas Bureau of Economic Geology.

McNeill, J., 1980, Electromagnetic terrain conductivity measured at low induction numbers: 788, Geonics Limited Ontario, Canada.

Nabighian, M. N. and J. C. Macnae, 1991, Time domain electromagnetic prospecting methods, *in* Nabighian M. N., Ed., Electromagnetic methods in applied geophysics Vol. 2, Applications: Sol. Expl. Geophys. Investigations in geophysics, no. 3, 427-509.

Nenna, V., D. Herckenrath, R. Knight, N. Odlum, and D. McPhee, 2013, Application and evaluation of electromagnetic methods for imaging saltwater intrusion in coastal aquifers: Seaside Groundwater Basin, California: Geophysics, **78**, no. 2, B77-B88.

Nielsen, P., 1990, Tidal dynamics of the water table in beaches: Water Resources Research, **26**, no.9, 2127-2134.

Nielsen, P., 1999, Groundwater dynamics and salinity in coastal barriers: Journal of Coastal Research, **15**, no. 3, 732-740.

Oppenheim, A., and R. Schafer, 2010, Discrete-time signal processing: Prentice Hall. (Third edition).

Paine, J. G., W. A. White, R. C. Smyth, J. R. Andrews, and J. C. Gibeaut, 2004, Mapping coastal environments with lidar and EM on Mustang Island, Texas, US: The Leading Edge, **23**, no. 9, 894-898.

Pincus, J. A., T. S. de Smet, Y. Tepper, and M. J. Adams, 2013, Ground-penetrating Radar and Electromagnetic Archaeogeophysical Investigations at the Roman Legionary Camp at Legio, Israel: Archaeological Prospection, **20**, no. 3, 175-188.

Santos, F. A., J. Triantafilis, K. E. Bruzgulis, and J. A. E. Roe, 2010, Inversion of multiconfiguration electromagnetic (DUALEM-421) profiling data using a one-dimensional laterally constrained algorithm: Vadose Zone Journal, **9**, no. 1, 117-125.

Seelig, W. N., and R. M. Sorensen, 1973, Investigation of shoreline changes at Sargent Beach, Texas: Texas A&M Univ. Sea Grant Pub. No. TAMU-SG-73-212.

Seijmonsbergen, A. C., D. T. Biewinga, and A. P. Pruissers, 2004, A geophysical profile at the foot of the Dutch coastal dunes near the former outlet of the 'Old Rhine', Netherlands: Journal of Geosciences/Geologie en Mijnbouw, **83**, no. 4, 287-291.

Stauble, D. K., J. M. Hubertz, R. J. Hoban, C. R. Livingston, and C. E. Pollock, 1994, Coastal studies in support of the Sargent Beach, Texas, erosion control project: US Army Corps of Engineers, Miscellaneous Paper CERC-94-3.

Todd, D. K., and L. W. Mays, 2005, Groundwater Hydrology: John Wiley & Sons, Inc, New Jersey.

Torrence, C., and G. P. Compo, 1998, A practical guide to wavelet analysis: Bulletin of the American Meteorological Society, **79**, no. 1, 61-78.

Vrbancich, J., 2009, An investigation of seawater and sediment depth using a prototype airborne electromagnetic instrumentation system- a case study in Broken Bay, Australia, Geophysical Prospecting, **57**, 633-651.

Weiss, C. P., and B. H. Wilkinson, 1988, Holocene cementation along the central Texas coast: Journal of Sedimentary Petrology, **58**, no. 3, 468-478.

West, G. F., and J. C. Macnae, 1991, Physics of the electromagnetic induction exploration method, in Nabighian M. N., Ed., Electromagnetic methods in applied geophysics Vol. 2, Applications: Sol. Expl. Geophys. Investigations in geophysics, no. 3, 5-45.

Weymer, B., M.E., Everett, T.S., de Smet, and C., Houser, 2015, Review of electromagnetic induction for mapping barrier island framework geology: Sedimentary Geology, **321**, 11-24.

Weymer, B., M.E., Everett, C., Houser, P., Wernette, and P., Barrineau, 2016, Differentiating tidal and groundwater dynamics from barrier island framework geology: Testing the utility of portable multifrequency electromagnetic induction profilers: Geophysics, **81**, no.5, E347-E361.

Won, I. J., D. A. Keiswetter, G. R. Fields, and L. C. Sutton, 1996, GEM-2: A new multifrequency electromagnetic sensor: Journal of Environmental and Engineering Geophysics, **1**, no. 2, 129-137.

APPENDIX

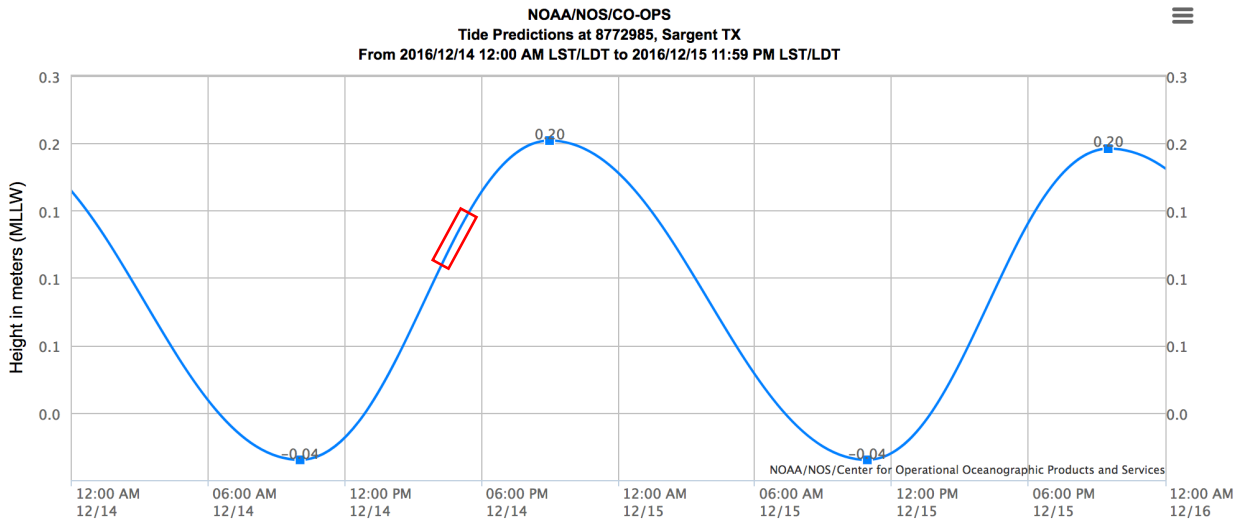

Date	Day of the Week	Time (LST/LDT)	Predicted (m)	High/Low
2016/12/14	Wed	10:01 AM	-0.04	L
2016/12/14	Wed	8:58 PM	0.19	H
2016/12/15	Thu	10:55 AM	-0.04	L
2016/12/15	Thu	9:31 PM	0.19	H

A-1: *Tidal chart for Sargent, TX Beach site used for time-series data, red block indicates time data was recorded (taken from NOAA).*

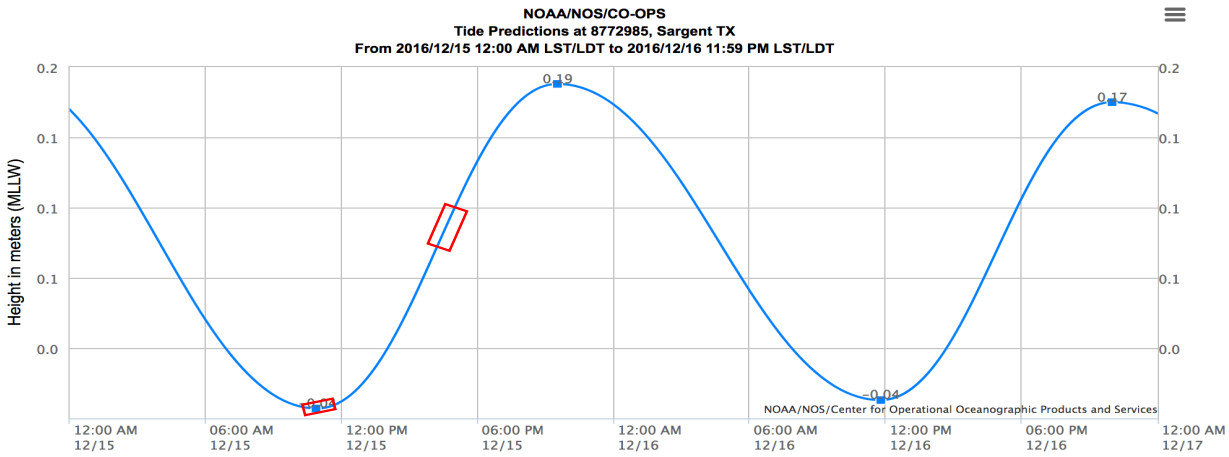

Date	Day of the Week	Time (LST/LDT)	Predicted (m)	High/Low
2016/12/15	Thu	10:55 AM	-0.04	L
2016/12/15	Thu	9:31 PM	0.19	H
2016/12/16	Fri	11:47 AM	-0.04	L
2016/12/16	Fri	9:59 PM	0.17	H

A-2: *Tidal chart for Sargent, TX Saltmarsh site used for time-series data, two red block indicate time data was recorded (taken from NOAA).*

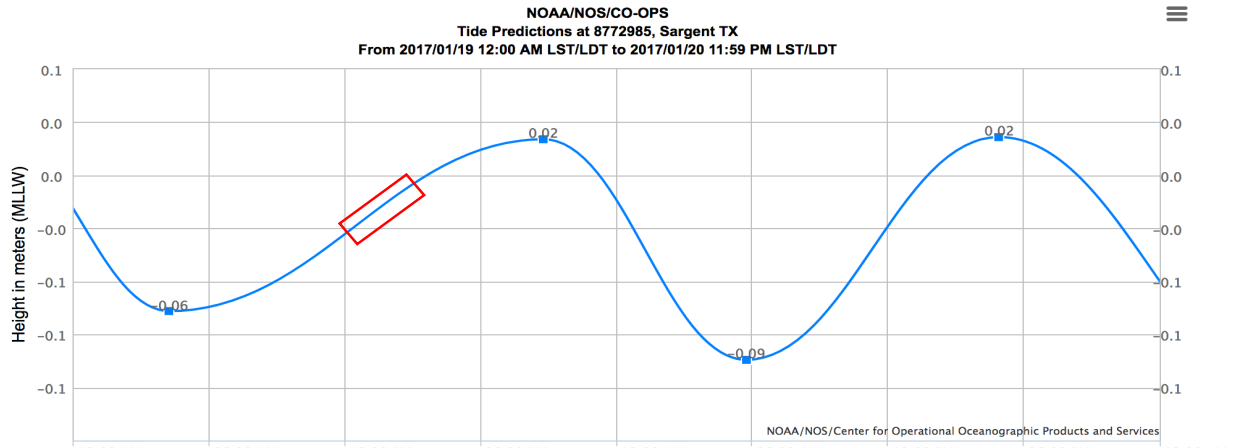

Date	Day of the Week	Time (LST/LDT)	Predicted (m)	High/Low
2017/01/19	Thu	04:14 AM	-0.07	L
2017/01/19	Thu	8:46 PM	0.01	H
2017/01/20	Fri	05:44 AM	-0.10	L
2017/01/20	Fri	4:53 PM	0.01	H

***A-3**: Tidal chart for Sargent, TX Saltmarsh site used for spatial profile data, red block is time data was recorded (taken from NOAA)..*

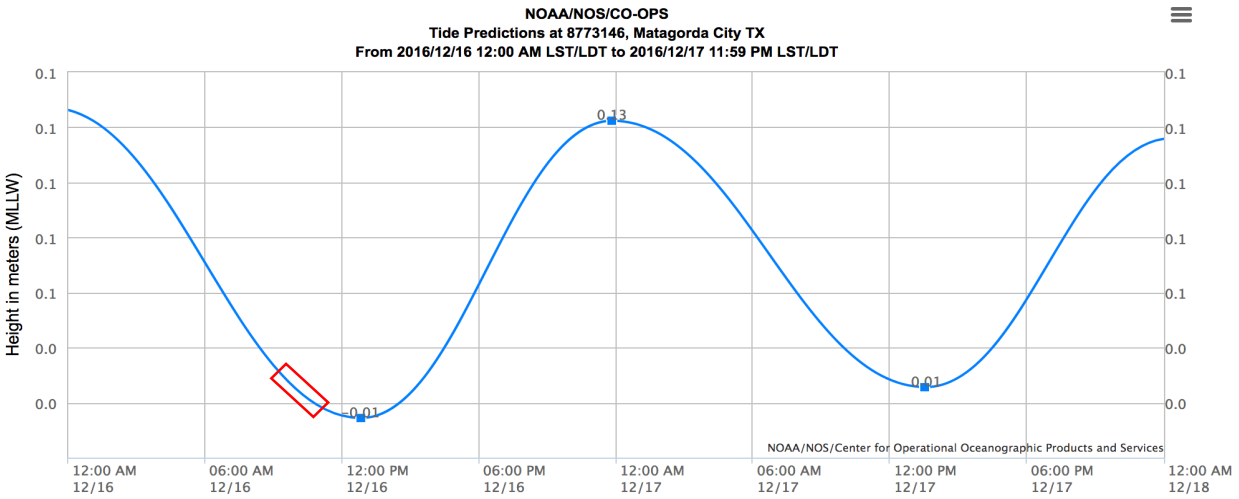

Date	Day of the Week	Time (LST/LDT)	Predicted (m)	High/Low
2016/12/16	Fri	12:49 PM	-0.01	L
2016/12/16	Fri	11:50 PM	0.13	H
2016/12/17	Sat	1:34 PM	0.01	L

A-4: Tidal chart for Matagorda, TX used for time-series data, red block indicates time data was recorded (taken from NOAA).

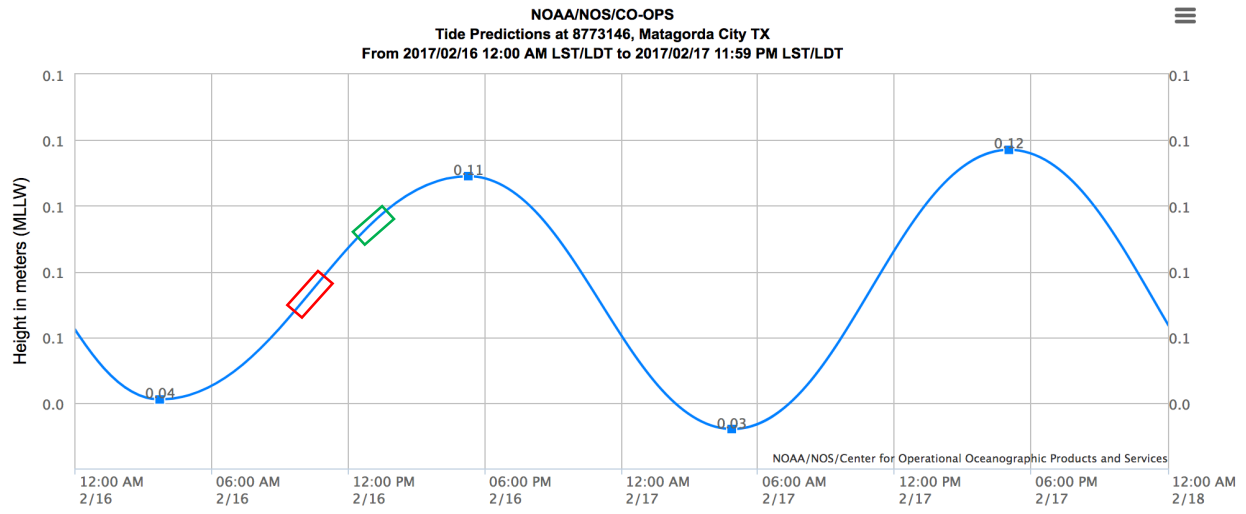

Date	Day of the Week	Time (LST/LDT)	Predicted (m)	High/Low
2017/02/16	Thu	03:42 AM	0.04	L
2017/02/16	Thu	5:16 PM	0.11	H
2017/02/17	Fri	04:52 AM	0.03	L
2017/02/17	Fri	5:01 PM	0.12	H

***A-5**: Tidal chart for Matagorda, TX used for spatial profile. Red block indicates time data was recorded for "There" trip, green block indicates time data was recorded for "Back" trip (taken from NOAA).*

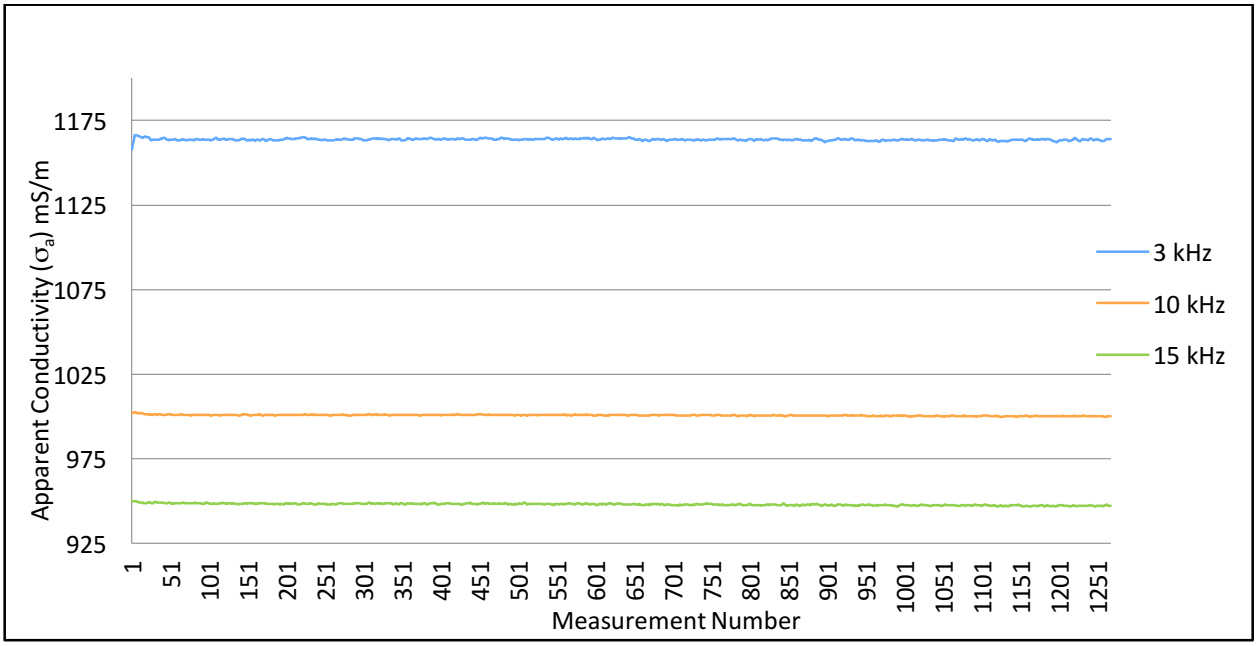

***A-6**: Sargent, TX beach time-series data plot.*

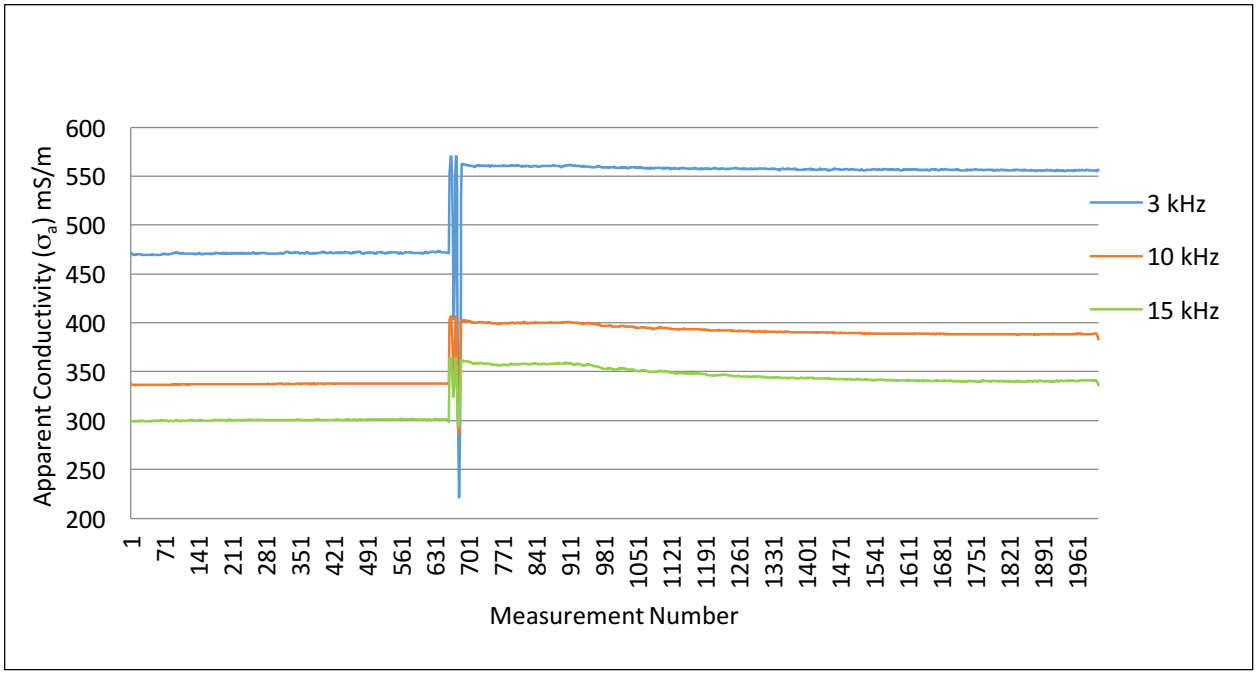

A-7: Sargent saltmarsh time-series data plot.

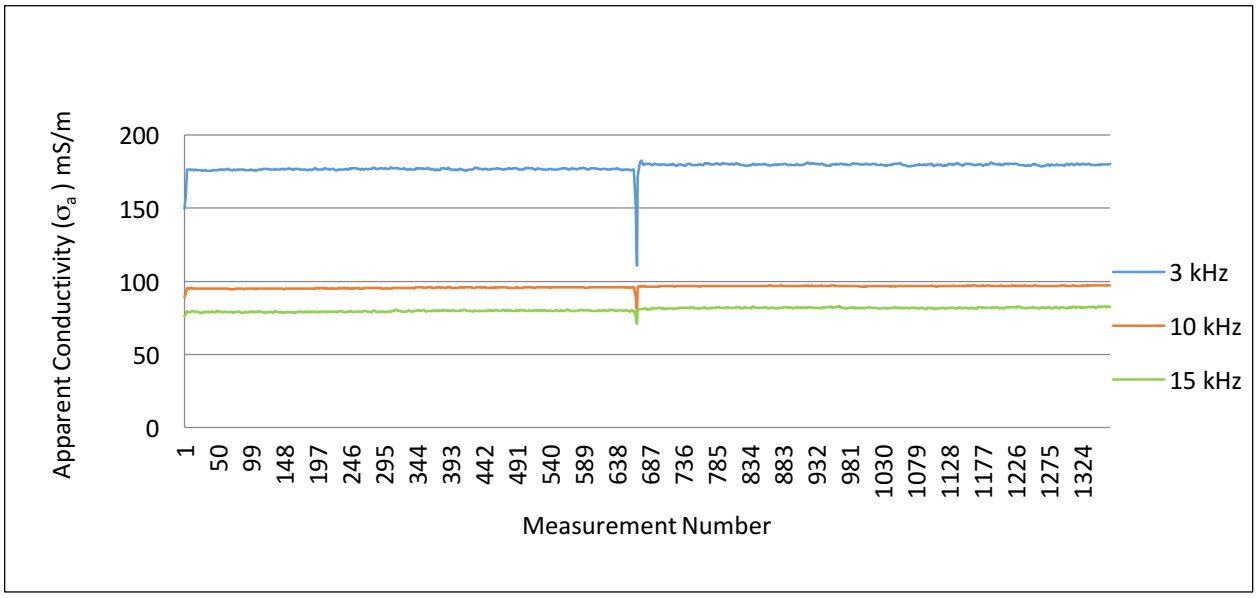

A-8: Matagorda Peninsula beach time-series data plot.

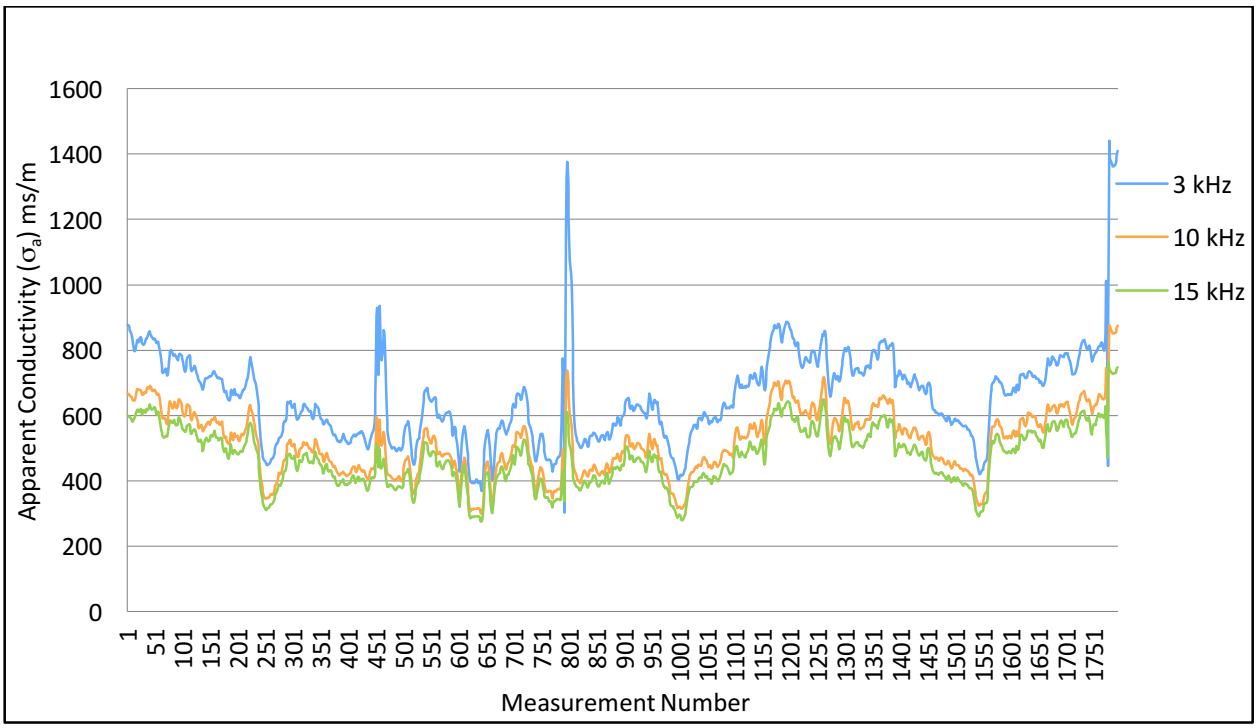

***A- 9**: Spatial Profile data plot for Sargent, TX saltmarsh, down main road to gate, south levee, and back (red path in Fig.4.2).*

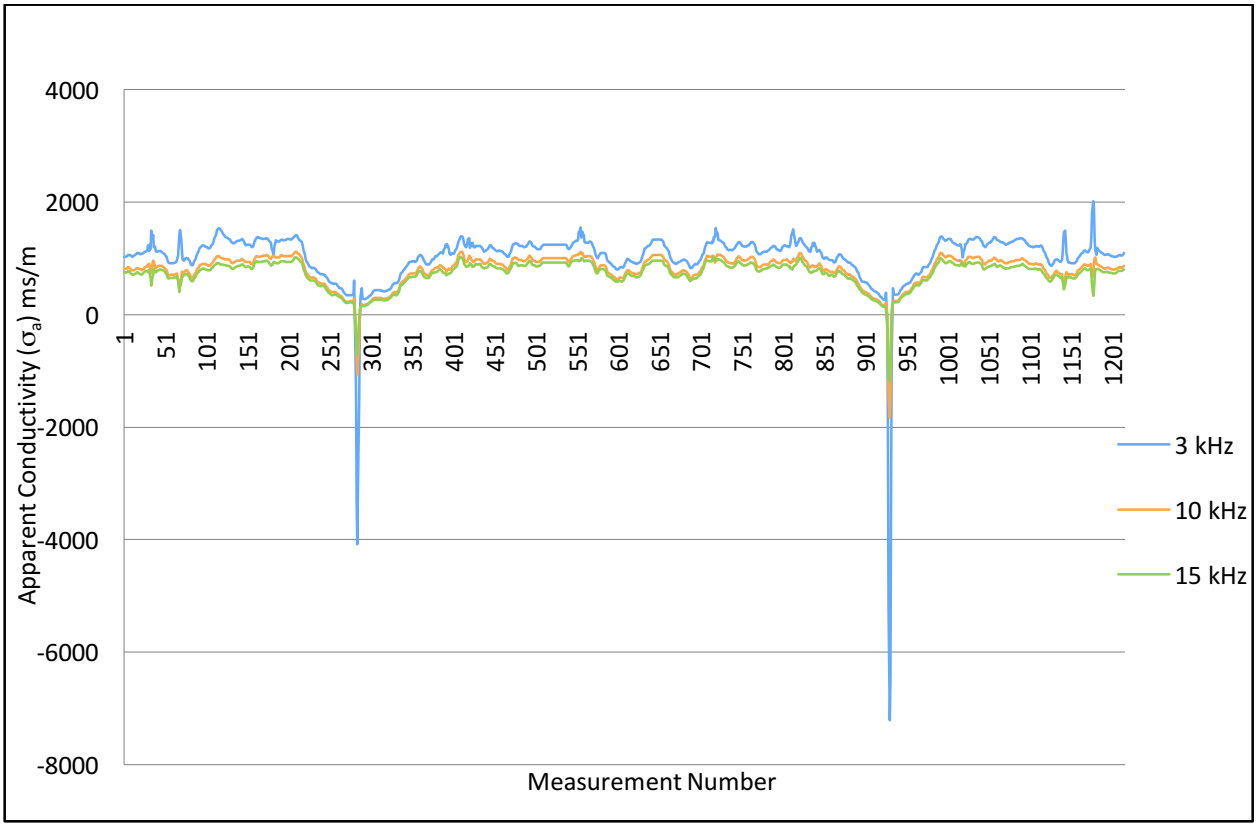

***A-10**: Spatial profile data plot for Sargent, TX saltmarsh, down main road, across bridge and back (purple path in Fig.4.2).*

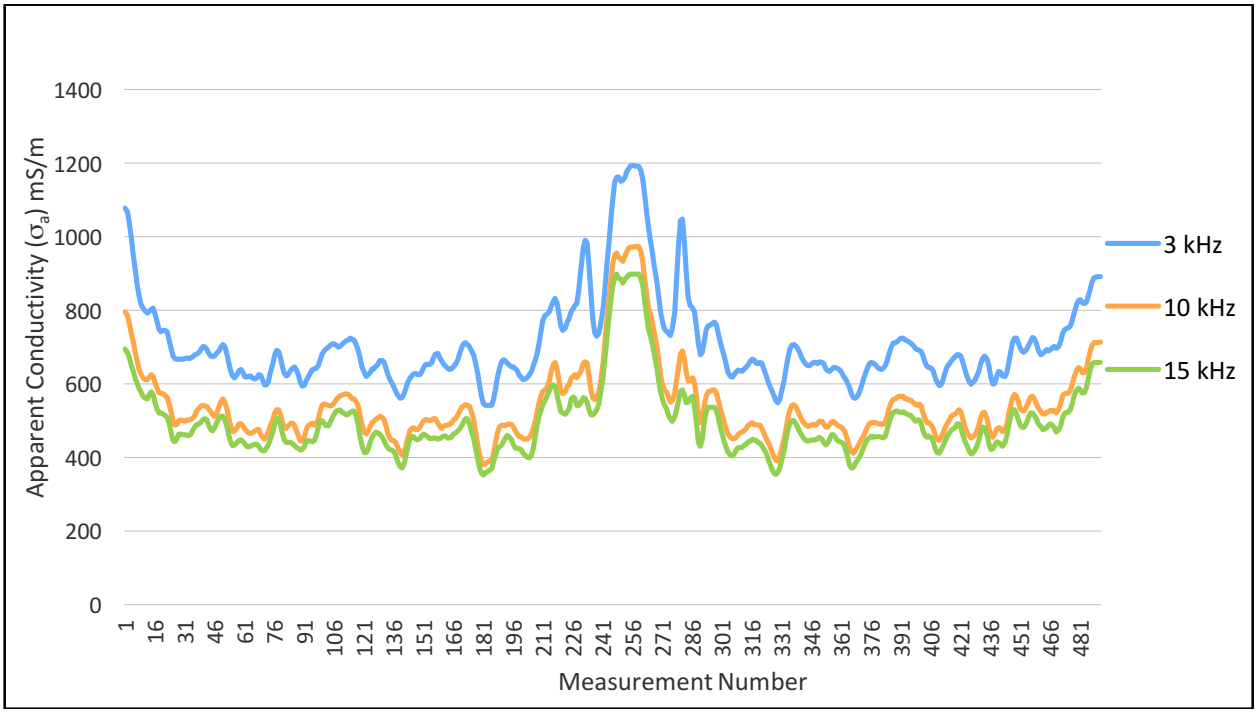

A-11: Spatial profile data plot for Sargent, TX saltmarsh, down north levee and back (blue path in Fig.4.2).

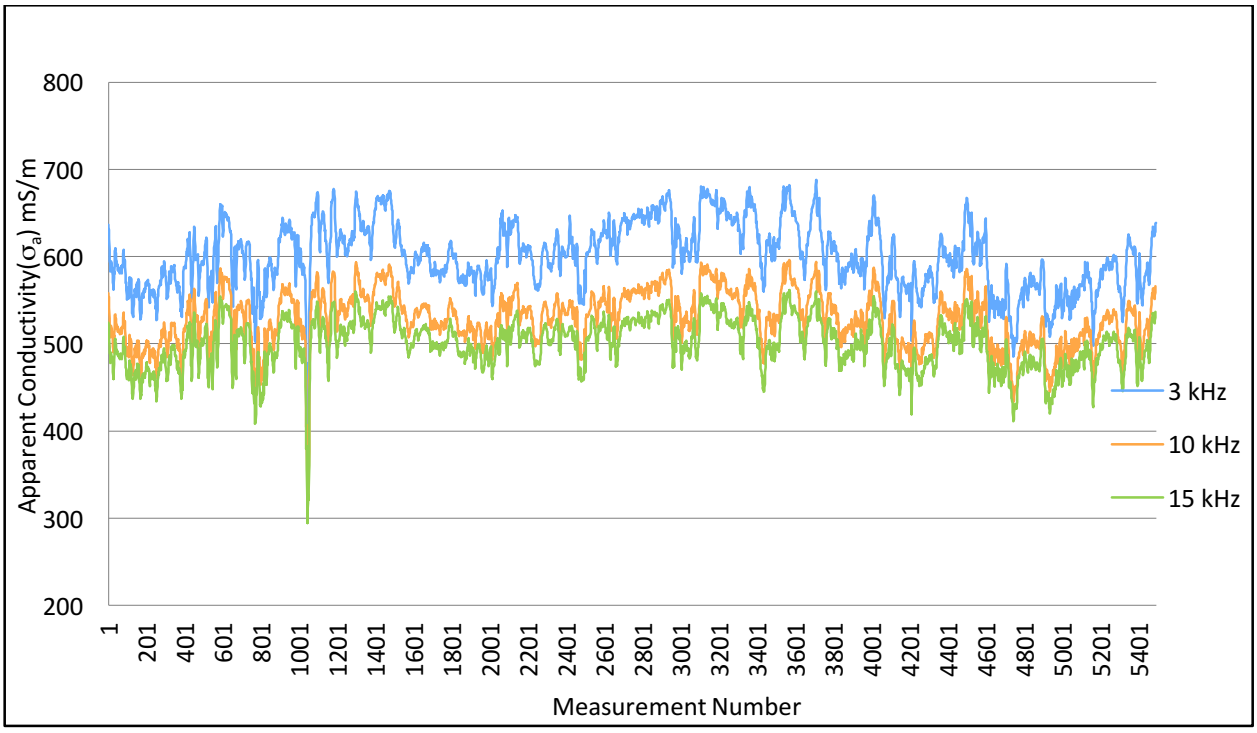

A-12: Spatial profile data plot for Matagorda Peninsula beach (there).

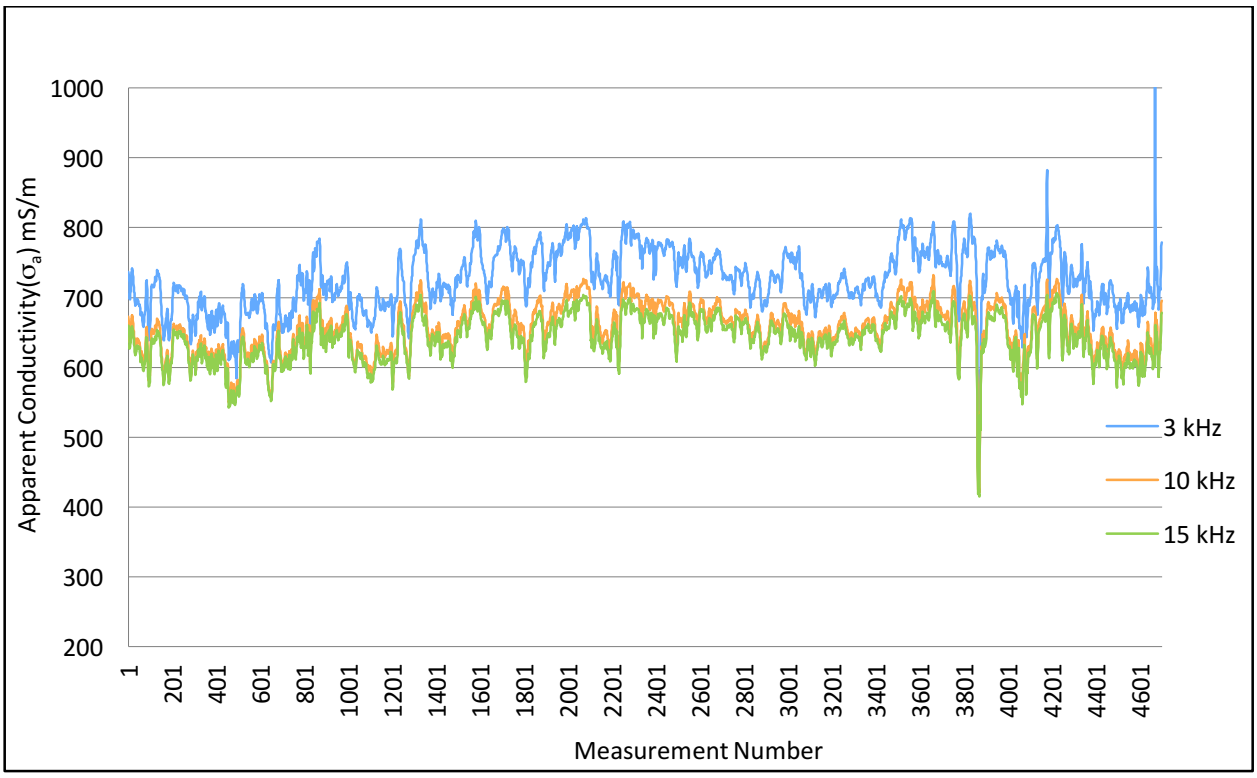

A-13: Spatial profile data plot for Matagorda Peninsula beach (way back).

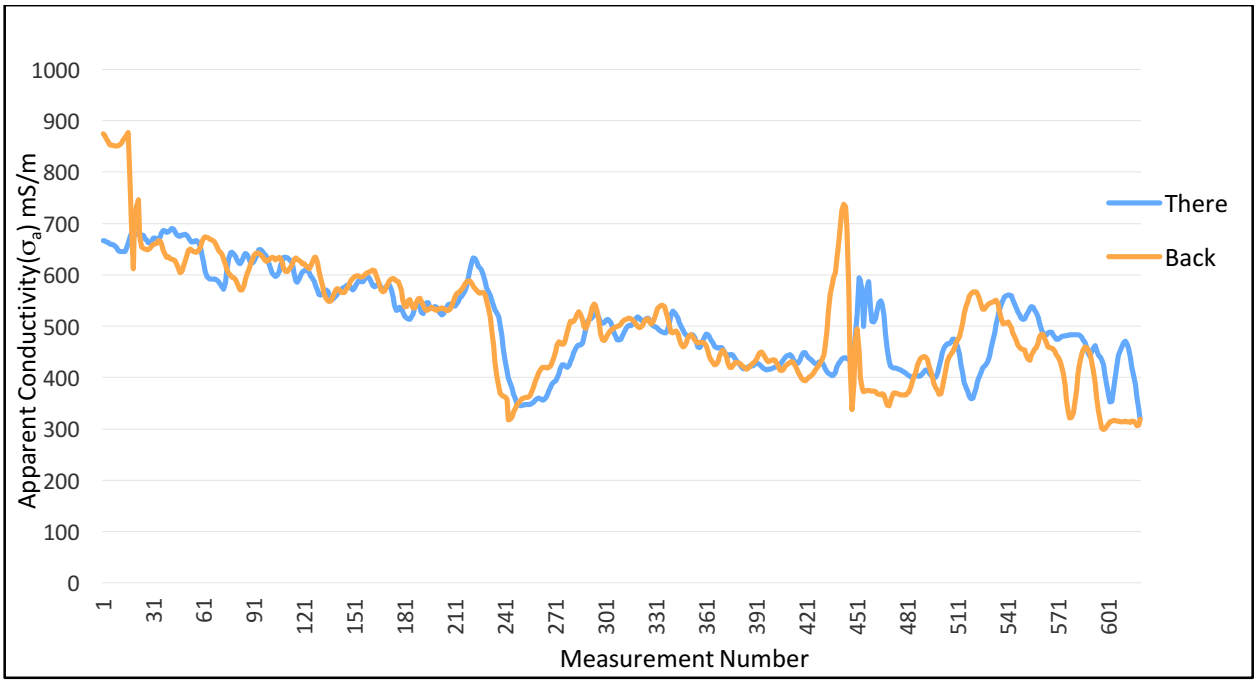

A-14: Repeatability graph (10 kHz) for Sargent, TX saltmarsh. Down main road to gate and back (red in Fig.4.3).

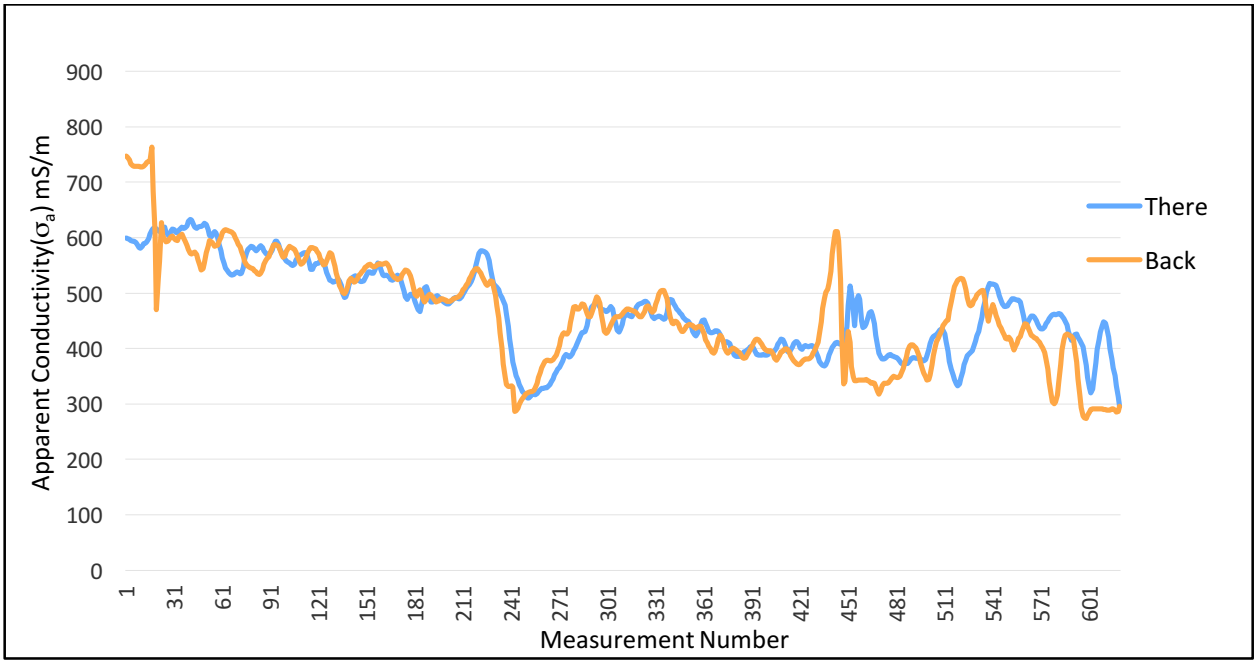

***A-15**: Repeatability graph (15 kHz) for Sargent, TX saltmarsh. Down main road to gate and back (red in Fig 4.3).*

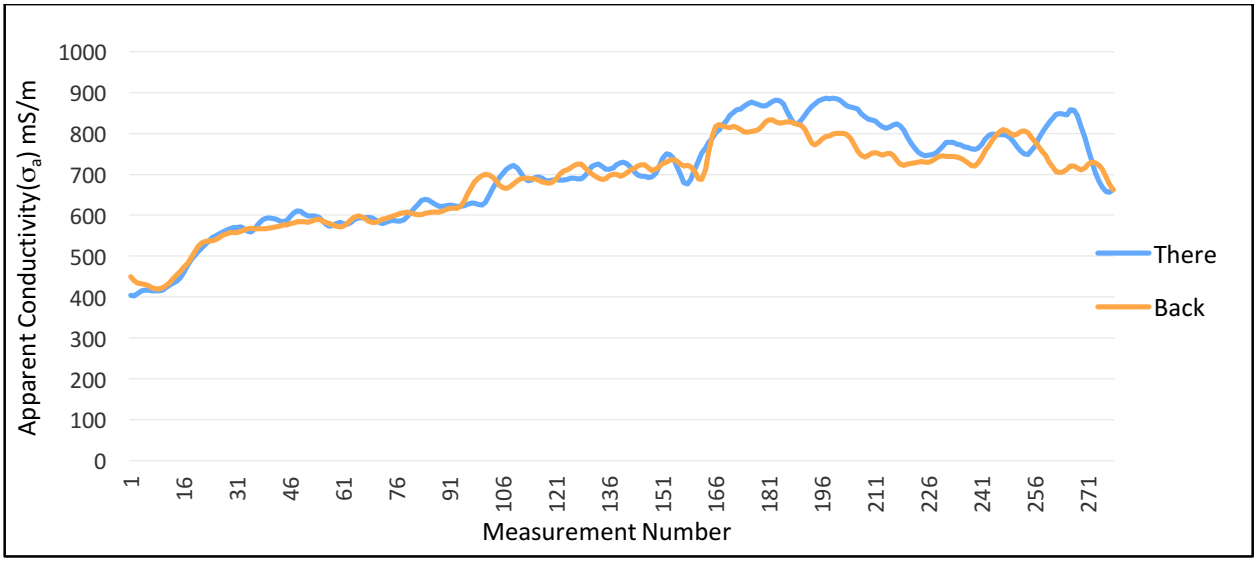

***A-16**: Repeatability graph (3 kHz) for Sargent, TX saltmarsh. Down south levee and back (yellow in Fig. 4.3).*

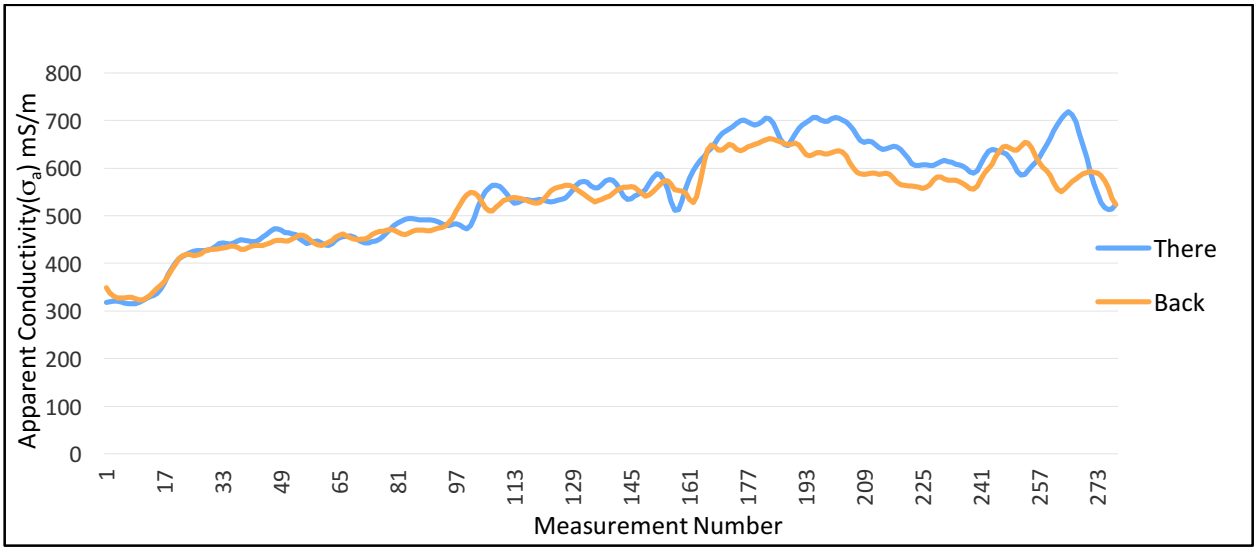

A-17: Repeatability graph (10 kHz) for Sargent, TX saltmarsh. Down south levee and back (yellow in Fig. 4.3).

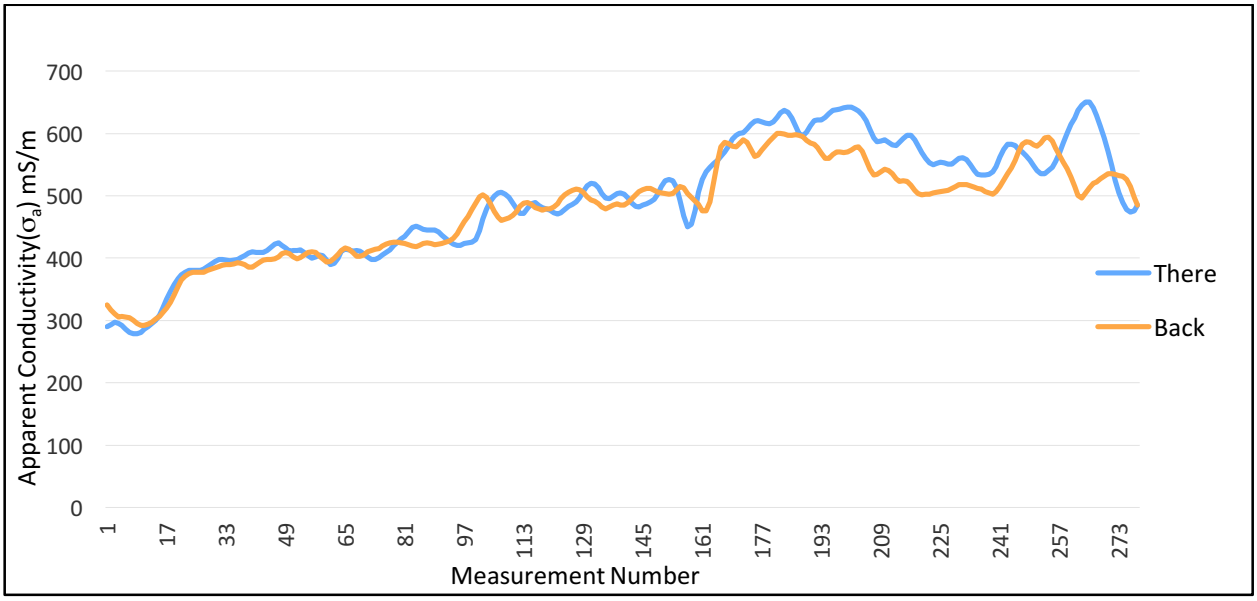

A-18: Repeatability graph (15 kHz) for Sargent, TX saltmarsh. Down south levee and back (yellow in Fig. 4.3).

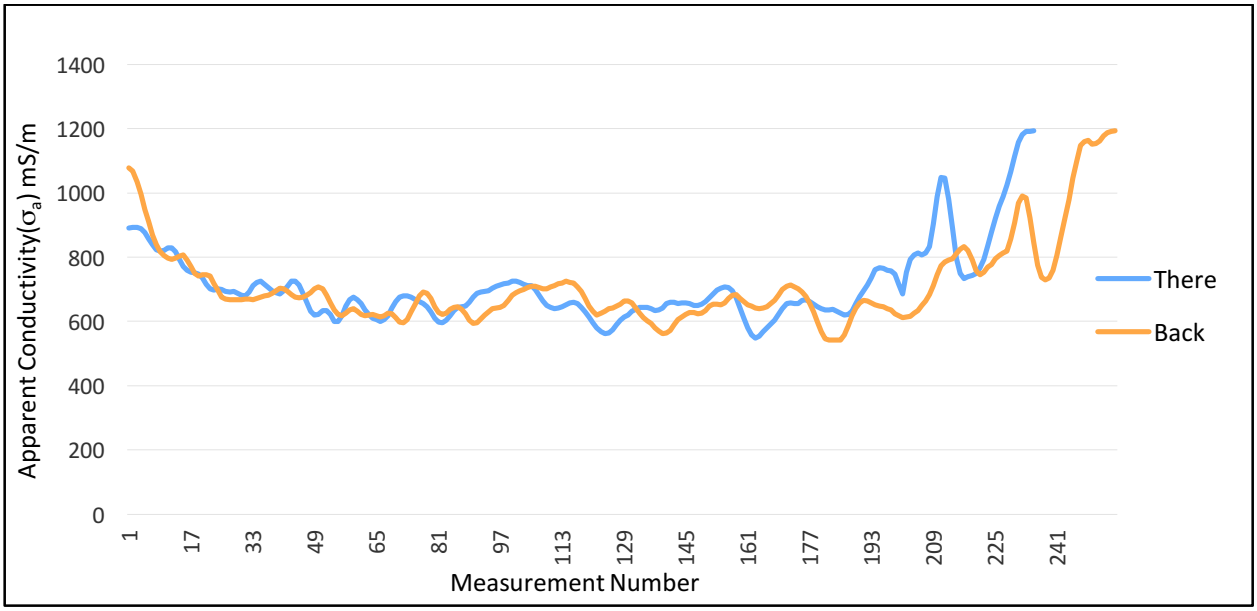

***A-19**: Repeatability graph (3 kHz) fro Sargent, TX saltmarsh. Down north levee and back (blue in Fig. 4.3).*

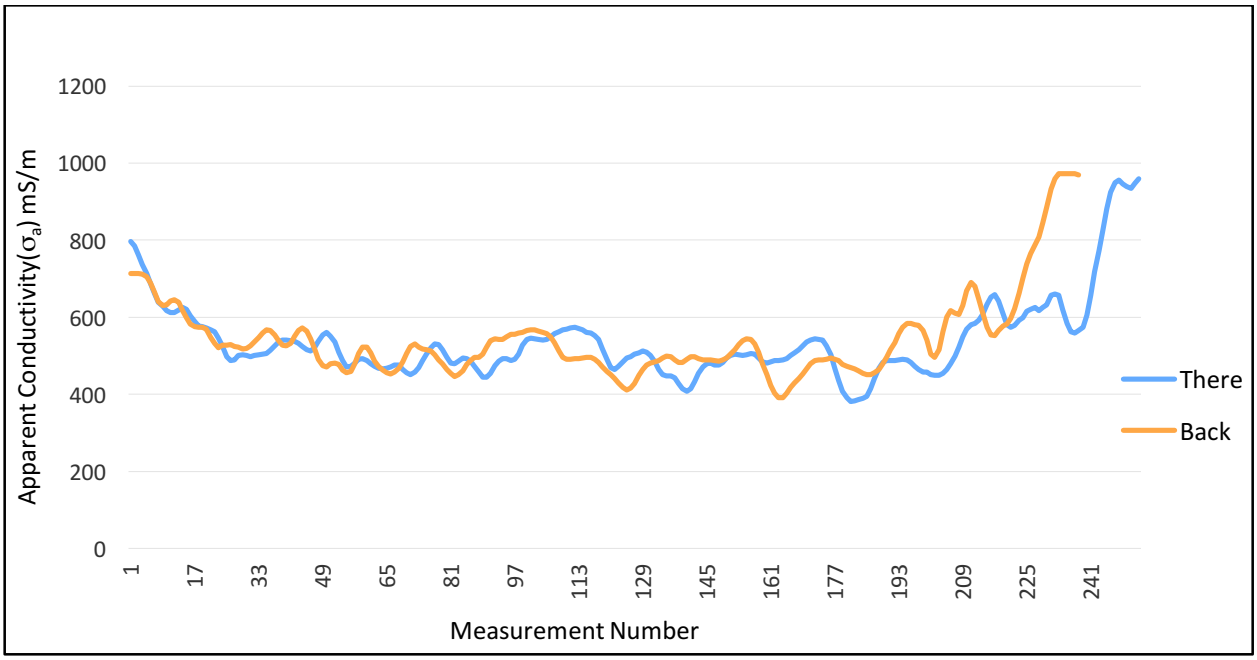

***A-20**: Repeatability graph (10 kHz) fro Sargent, TX saltmarsh. Down north levee and back (blue in Fig. 4.3).*

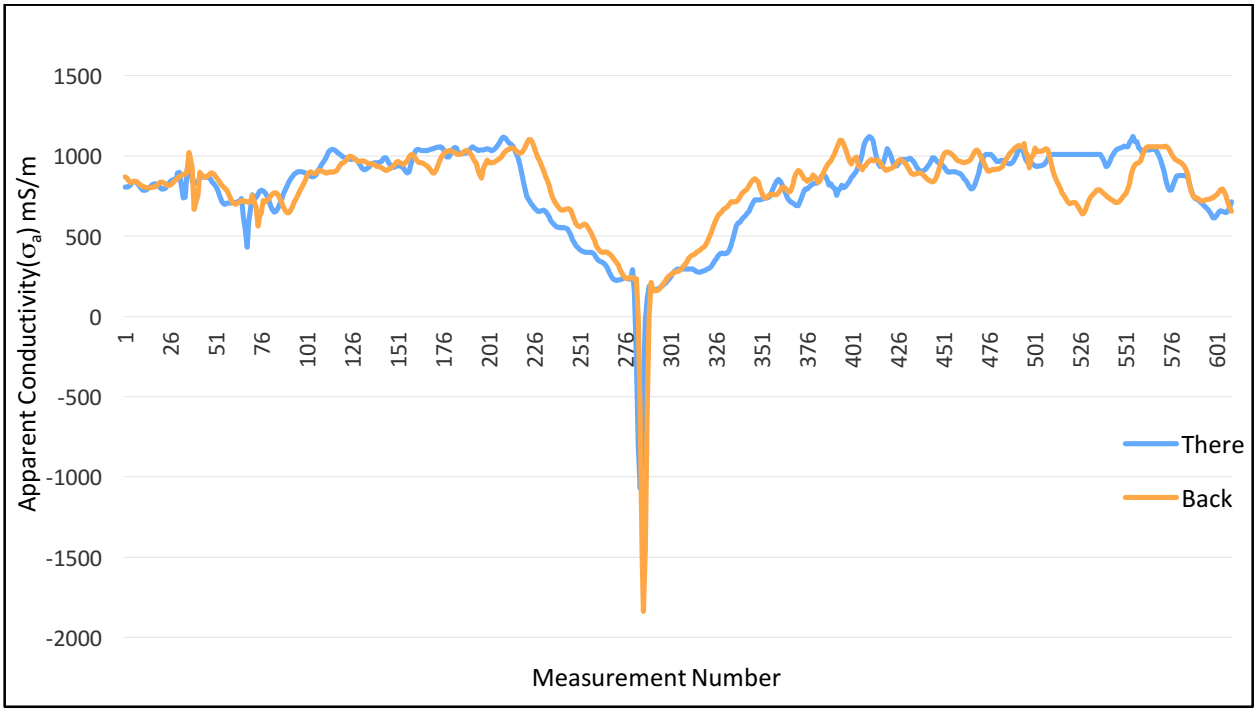

***A-21**: Repeatability graph (10 kHz) for Sargent, TX saltmarsh. Down main road across bridge and back (purple in Fig. 4.3).*

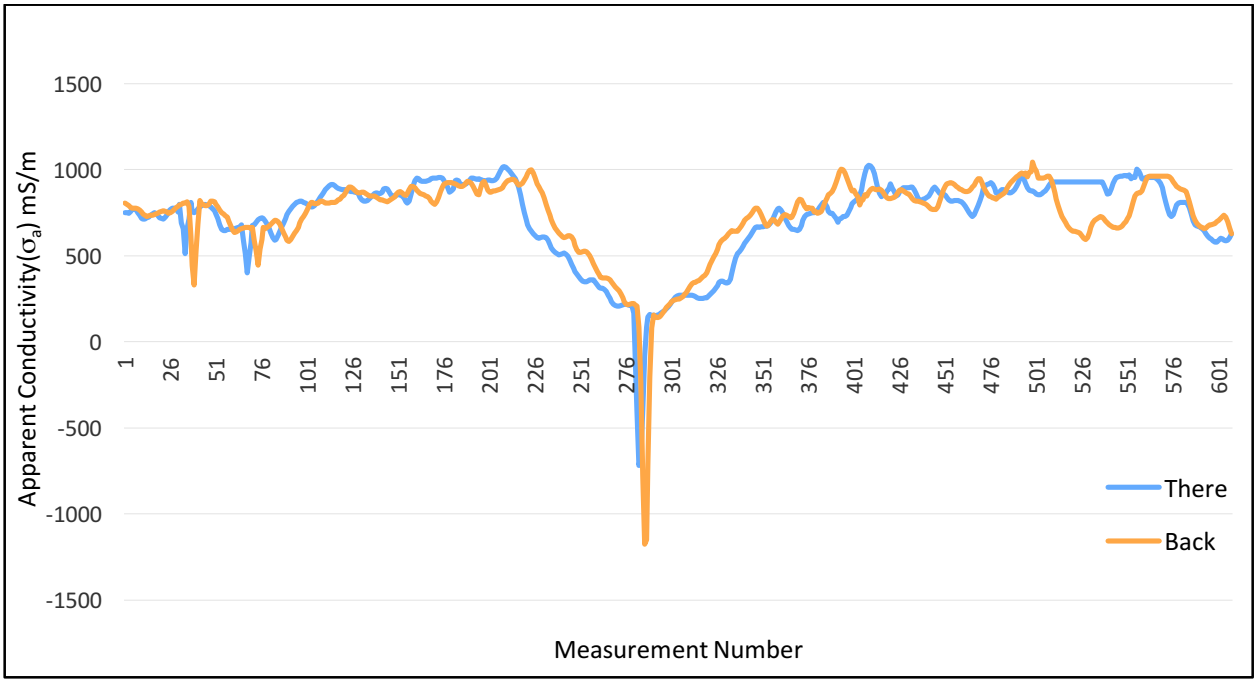

***A-22**: Repeatability graph (15 kHz) for Sargent, TX saltmarsh. Down main road across bridge and back (purple in Fig. 4.3).*

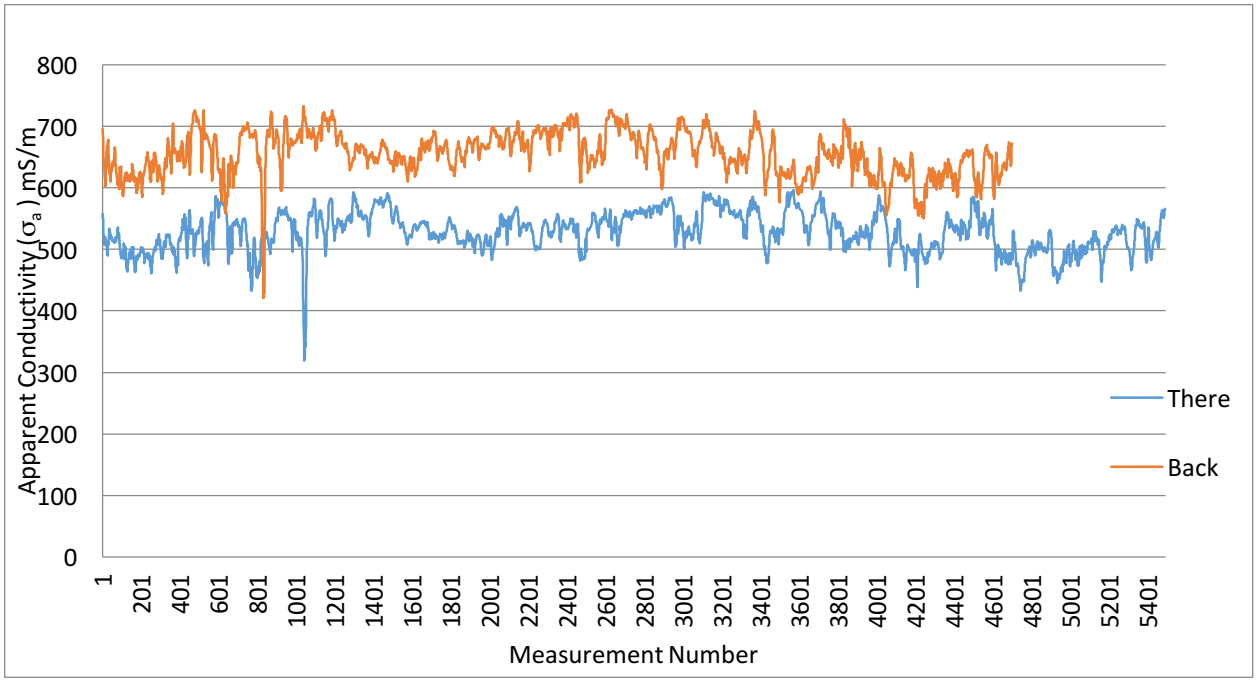

***A-23**: Repeatability graph (10 kHz) for Matagorda Peninsula (path shown in Fig. 3.3).*

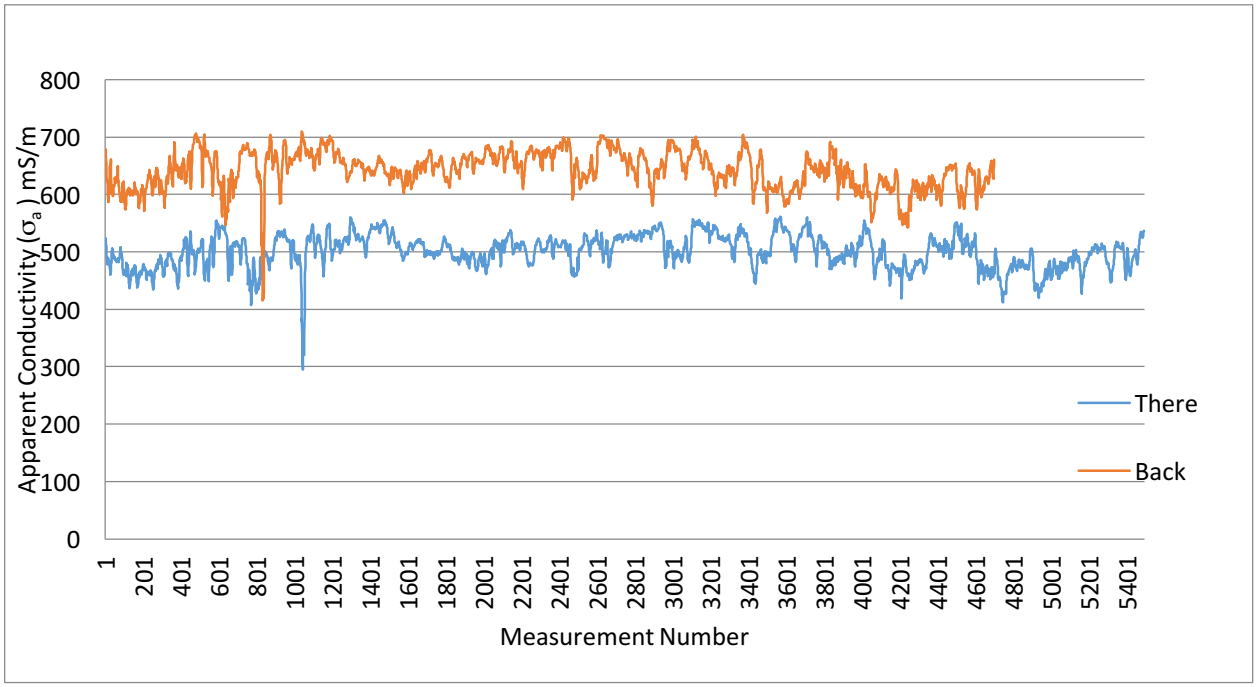

***A-24**: Repeatability graph (15 kHz) for Matagorda Peninsula (path shown in Fig. 3.3).*